# Atmospheric pressure plasma engineered superhydrophilic CuO surfaces with enhanced catalytic activities.

Avishek Dey[a], Gauthaman Chandrabose[a], Paheli Ghosh[a], Lois A.O Damptey[a], Adam H. Clark[b], Vimalnath Selvaraj[c], Ramachandran Vasant Kumar [c], Nicholas St. J. Braithwaite[a], Siarhei Zhuk[d], Goutam Kumar Dalapati[a,e,f,*] Seeram Ramakrishna[f], Satheesh Krishnamurthy[a,*]

a. School of Engineering and Innovation, The Open University, Milton Keynes, MK76AA, UK
b. Paul Scherrer Institut, Forschungsstrasse 111, 5232, Villigen, Switzerland
c. Department of Materials Science and Metallurgy, University of Cambridge, Cambridge, CB3 0FS, UK
d. Institute of Materials Research and Engineering, A*STAR (Agency for Science, Technology and Research), 2 Fusionopolis Way; Innovis, #08-03, Singapore 138634
e. Department of Physics, SRM University – AP, Amaravati 522502, Andhra Pradesh, India
f. Center for Nanofibers and Nanotechnology, Faculty of Engineering, National University of Singapore, Singapore-1175

* satheesh.krishnamurthy@open.ac.uk

* goutam.d@srmap.edu.in

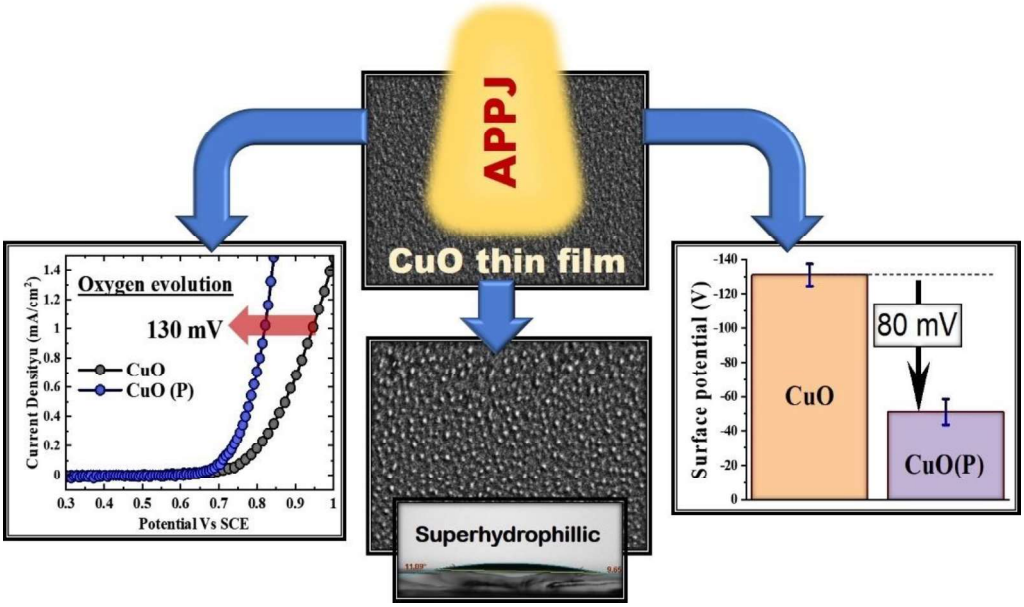


*Atmospheric pressure plasma functionalisation of CuO thin films transforms surfaces to superhydrophillic, lowers surface potential, boosts electro and photo catalytic activities*.

**Highlights**

- Fast and environment friendly route to engineer CuO thin film surfaces.
- Low power atmospheric pressure plasma jet transforms CuO surface superhydrophilic.
- Plasma functionalisation boosts electro and photocatalytic activities.
- Presence of oxygen radicals critical for the enhanced activities.
- Energetic species in plasma perturbs the local electronic and lattice structure.

**Abstract**

Cupric oxide (CuO) thin film has found widespread application as a low-cost, earth-abundant material for electro and photo catalytic applications. High surface wettability is a key factor to achieve enhanced efficiency in these catalytic applications. Here, we report a fast and environment friendly route to fabricate super hydrophilic CuO thin films using a low power (5 to 10 Watts) atmospheric pressure plasma jet (APPJ). With APPJ treatment for 5 minutes, the CuO surface transforms from hydrophobic to super-hydrophilic with threefold increase in catalytic activity. The electrodes were extensively characterized using various bulk and surface-sensitive techniques. APPJ introduces anisotropy in the crystal structure and creates unique three-dimensional surface morphology with distinct surface chemical and electronic features. Interestingly, presence of oxygen in the plasma was found to be critical for the enhanced activities and the activity decreased when the functionalised with nitrogen plasma. Oxygen plasma functionalisation of CuO electrodes resulted in a 130 mV reduction in the onset potential for oxygen evolution reaction along with enhanced current density ,10 mA $cm^{-2}$ against 3 mA $cm^{-2}$ at 1 V vs Saturated Calomel Electrode in 0.1M KOH without *iR* compensation. Importantly, without introducing any external dopants the work function could be decreased by 80mV. Moreover, the treated films exhibited a higher rate of photo degradation (0.0283 $min^{-1}$ compared to 0.0139 $min^{-1}$) of Methylene Blue and phenol indicating efficient charge separation. This work presents the potential of APPJ functionalisation of CuO surface to boost the activity of other thin film catalyst materials and solutions processed systems.

**Keywords:** CuO, OER, plasma jet, surface functionalization, Phenol degradation.

## 1. Introduction

The increasing concerns about global energy crisis has triggered the search for alternate sources of energy which are environment-friendly and cost-effective for largescale implementation. Electrochemical splitting of water into oxygen and hydrogen is one of the most promising and sustainable strategies for producing hydrogen as a clean source of energy for zero carbon emissions.[1] Electrocatalytic splitting of water consists of two crucial half-cell reactions, oxygen evolution reaction (OER) at the anode and hydrogen evolution reaction (HER) at the cathode. However, to achieve high efficiency in $H_2$ production from electrocatalytic water splitting, it is important to circumvent the issue of slow reaction kinetics during OER at the anode as it requires potential much higher than the theoretical value of 1.23 V.[2] Typically, OER involves the loss of four electrons and four protons from two water molecules to form a single $O_2$ molecule.

$$2H_2O \longrightarrow 4e^- + 4H^+ + O_2 \quad (1)$$

To date, oxides of iridium and ruthenium ($IrO_2$, $RuO_2$) have shown the best performance towards OER, because of their excellent catalytic activity in both low and high pH conditions.[3,4] However, the low-abundance and high-cost of these materials are a detriment to their widespread applications. Therefore, it is imperative to develop efficient OER catalysts that are cheap, earth-abundant, stable in electrolyte and can be operated at low over potentials for OER. Recently, extensive research is being carried out on the oxides of "non-noble" transition metals as electrode materials for OER. Several transition metals along with their alloys have also been well studied. [5–7] Copper has emerged as an ideal candidate for water

oxidation electrodes due to its low cost, earth-abundance and rich redox properties. Several Cu based nanostructured oxides and model complexes have been reported as electrocatalysts. [8] However, the OER activities of Cu oxides suffer from high onset potential (320 and 450 mV), and the challenge lies in reducing these values. [5,9] Several approaches have been designed with the aim of lowering the over-potential values that can be comparable to Co and Ni catalysts. Techniques such as electrochemical deposition, evaporation, sol gel, thermal oxidation and sputter deposition have been widely used for synthesis of CuO thin films.[10–14] However, most of these synthesis techniques require high temperature annealing of the films for durations ranging from 2 to 4 hours to improve crystal quality./crystallinity. Previous publications by some of the authors have demonstrated that high temperature annealing enhances the catalytic activity of CuO electrodes. [15–17]. Hence, it is required to develop faster and more energy-efficient strategies towards the synthesis of efficient, ~~low-cost~~ and earth abundant OER catalysts. Lately, plasma technology has emerged as a highly efficient tool for enhancing the catalytic activity of wide range of organic and inorganic materials.[18–27] Non-thermal plasmas have high electron temperature but low gas temperature and consist of abundant chemically active species for reaction with different surfaces.[28] Mistry *et al*. reported a 350 mV reduction in onset potential for $CO_2$ reduction using copper oxide nanostructures grown on polycrystalline Cu with oxygen ($O_2$) and hydrogen ($H_2$) plasmas .[24] Similar work by Gao and co-workers resulted in increased selectivity towards ethylene, ethanol, and n-propanol during Carbon Dioxide Electroreduction via low-pressure plasma pre-treatments of Cu nanocubes.[25] Plasma technology can be exploited for creating lattice defects and oxygen vacancies, introducing subsurface oxygen species, tuning the surface electronic states, doping and structural modifications in materials which has reportedly enhanced the activity of electrocatalysts.[29]

However, the afore-mentioned plasma techniques were in low-pressure regime, thus, requiring sophisticated vacuum equipment. Out of the various non-thermal plasma sources, atmospheric pressure plasmas have gained attention for materials processing, as they are independent of vacuum equipment ~~which reduces the material processing cost~~ and can be used for inline large-scale applications.[30] Additionally, atmospheric pressure plasma jets (APPJ) are not restricted within the dimensions of the electrodes and can be directed towards 2 dimensional (2D) or 3D substrates.[31] APPJs consist of charged particles, neutral metastable species, radicals, and radiations in the UV and visible regions and is a solvent-free, environment-friendly alternative to engineer the surface electronic and chemical properties of catalyst materials .[30,32] Recently, we have been able to synthesise $Cu_2O$/CuO heterojunction catalysts with low density of interfacial defects using APPJ induced surface functionalisation.[33] The CuO thin film has attracted enormous attention due to its hydrophobic properties. Development of superhydrophobic CuO surface is much sought-after for microelectronic applications.[34] Hydrophilicity is a necessary for various applications e,g. heat transfer , microfluidics, oil–water separation, photothermal conversion, catalysis etc.[35–37] Hence, ability to engineer CuO thin films to be super hydrophilic in nature, will have far reaching applications such as self-cleaning and antireflective coatings, antifogging films, thin film devices, spray coating, heat transfer, separation membranes and smart surfaces with reversible switching abilities.[38] Techniques like high temperature annealing (450 C for 3hour), low pressure oxygen plasma treatment have been used to transform hydrophobic CuO surfaces to super-hydrophilic.[39,40] Recently we have reported ultra-thin ultrathin *p*- type cupric oxide (CuO) enhances the performance and stability of solution- processed CZCTS thin films Solar Cells. [41] Plasma functionalisation of this CuO intermediate layer could be an effective approach to enhance the efficiencies of similar solution processed devices, where surface hydrophilicity dictates the interfacial charge transfer between layers. In this article we

present an environment-friendly route towards fabricating super hydrophilic CuO thin films with enhanced electro and photo catalytic activities using APPJ surface functionalizing technique.

## 2. Experimental Details

### 2.1 Electrode preparation

CuO thin films were deposited on fluorine doped tin oxide (FTO) glass substrates using magnetron sputtering. All substrates were initially cleaned by ultrasonication in isopropanol (IPA) for 10 mins followed by drying in a nitrogen gas flow. Subsequently, the substrates were transferred to the sputtering chamber where CuO thin films were deposited in argon ambient at room temperature using a stoichiometric CuO target. Prior to deposition the chamber was pumped to high vacuum ($6 \times 10^{-4}$ mTorr) and then operated at 3 mTorr working pressure. The sputtering rate was optimized to achieve CuO films of average thickness 300 ± 30 nm.

The sputtered CuO films were annealed at 375 °C on a hot plate in an ambient atmosphere and simultaneously exposed to an APPJ for 5 minutes. The films were kept at a distance of 5 mm from the electrodes to avoid arcing between the sample and electrodes surface. [42] The plasma jet was operated at a frequency of 13.56 MHz and 12 dBm Radio frequency (RF) level. With helium as the carrier gas, flowing at 3 standard liters per minute (slm) mixed with oxygen or nitrogen (1% of helium). The input power was adjusted to 10 watts and 5 watts for different samples. Details of the plasma jet can be found in our previous article.[30] The catalytic properties were then compared between as deposited copper oxide (CuO), copper oxide annealed at 375 °C for 5 mins [CuO(A)] and plasma functionalized CuO with simultaneous annealing for 5 mins [CuO(P)].

## 2.2 Material Characterization

Water contact angle (CA) was measured using attention Theta Lite optical tensiometer with high purity distilled water. Surface morphology of the thin films were investigated using the Zeiss Supra 55VP scanning electron microscope (SEM). X-ray diffraction (XRD, M/s. BRUKER D8 Advance) pattern for all samples was recorded in the 2θ range of 20-50° using Cu-Kα radiation (λ = 0.154060 nm) with a scan rate of 0.5° min-1 at 40 kV and 40 mA. Raman spectra were acquired on Horiba Jobin-Yvon LabRAM HR evolution spectrometer using an $Ar^+$ laser (514.5 nm) as the excitation source**.** The electronic properties of as-prepared, furnace-annealed and 10W plasma treated copper oxide samples were probed using X-ray photoelectron spectroscopy (XPS) with a load-locked KRATOS XSAM-800 instrument equipped with a dual anode X-ray source using a Mg Kα (1253.6 eV) excitation source operated at 12 kV and 10 mA. The high magnification analyser mode was chosen to collect electrons from the smallest possible area on the specimen, ~ 4.0 $mm^2$, for Cu 2*p*, Cu *LMM*, O 1*s* core levels and the valence band. All XPS spectra were analysed using CasaXPS software (version 2.3.16). Base pressure of the analysis chamber was maintained below $10^{-9}$ mbars throughout the measurements. ~~The XPS spectra were analysed using CasaXPS software (version 2.3.16).~~ The acquired spectra were aligned with respect to the binding energy position of C 1*s* peak of adventitious carbon at 285.0 eV. All core lines were fitted with a combination of Gaussian and Lorentzian line shape (30% Lorentzian) after Shirley background subtraction to keep the fitting residue ($\chi 2$) <1. Kelvin probe force microscopy (KPFM) was performed using an Asylum Research MFP-3D with Pt−Ir-coated conducing silicon probes (PPP-EFM, Nanosensors). The tip was biased at +3 V. The surface potential map was acquired on an area of 25 $\mu m^2$ with scan rate of 1 Hz and 512 points and lines.

Ex-situ X-ray absorption spectroscopy measurements were carried out at the SuperXAS beamline of the Swiss Light Source. [43] The storage ring operated at 2.4 GeV in top-up mode

with a ring current of 400 mA. The polychromatic X-ray beam from a 2.9 T bending magnet was collimated by a silicon-coated mirror (which also served to reduce higher-order harmonics) and subsequently monochromatised by a Si(111) channel-cut monochromator for the Cu K edge XAS measurements. The data were collected in quick-scanning extended X-ray absorption fine-structure spectroscopy (QEXAFS) mode at 1 Hz in fluorescence mode utilising a PIPS fluorescence detector.[44] A Cu reference foil was measured for absolute energy calibration. The data were processed using ProQEXAFS to extract, calibrate, normalise and average. [45] The fitting of the extended X-ray absorption fine structure (EXAFS) was performed using the Demeter suite. [46]

**2.3 Electrocatalytic and Photocatalytic measurements**

All the electrochemical tests were performed in a conventional three-electrode system using Autolab PGSTAT M204 potentiostat/galvanostat equipped with a FRA32M. The configuration consisted of Pt counter electrode, saturated calomel (4M KCl) electrode (SCE) as the reference electrode and CuO thin films as working electrode in 0.1 M KOH (pH 13). Current was collected using Copper wires attached to the base of FTO using silver paste. A square active area was created by covering the substrates with polypropylene tapes, thus, preventing any electrolyte leakage. Linear sweep voltammetry (LSV) was performed at a scan rate of 1 mV $s^{-1}$ after the system achieved equilibrium. Electrochemical impedance spectroscopy (EIS) was performed over the frequency range of 0.1 Hz to 100 kHz and 10 mV amplitude at an applied potential of 0.5 V vs SCE.

The photocatalytic activity of CuO, CuO(A), and CuO(P) was evaluated by monitoring the level of degradation of Methylene Blue (MB) dye irradiated under xenon light source (M/s. Asahi Spectra, HAL 320). Thin-film samples having an area of 1.5 $cm^2$ were placed inside the reactor vessel containing 20 mL of MB solution (10 mg $L^{-1}$ in deionized water), and the dye

solution mixed with 1 ml of $H_2O_2$ (0.5 M). The light source (300 W, 75 mW $cm^{-2}$, 350-1100 nm, AM1.5G filter) was used to illuminate the samples vertically with a distance of 20 cm from the top surface of the dye solution. The intensity of the light source was tuned to attain 1 SUN condition, and the light illuminated area was maintained about 30mm x 30mm. During the 3 hours of light illumination, 1 mL aliquot of the MB solution was collected at a time interval of every 30 mins. The liquid samples are transferred into a quartz cuvette, and absorption spectra were recorded using a UV-vis spectrophotometer (M/s. Thermo Scientific, Evolution 220).

## 3. Results and Discussion

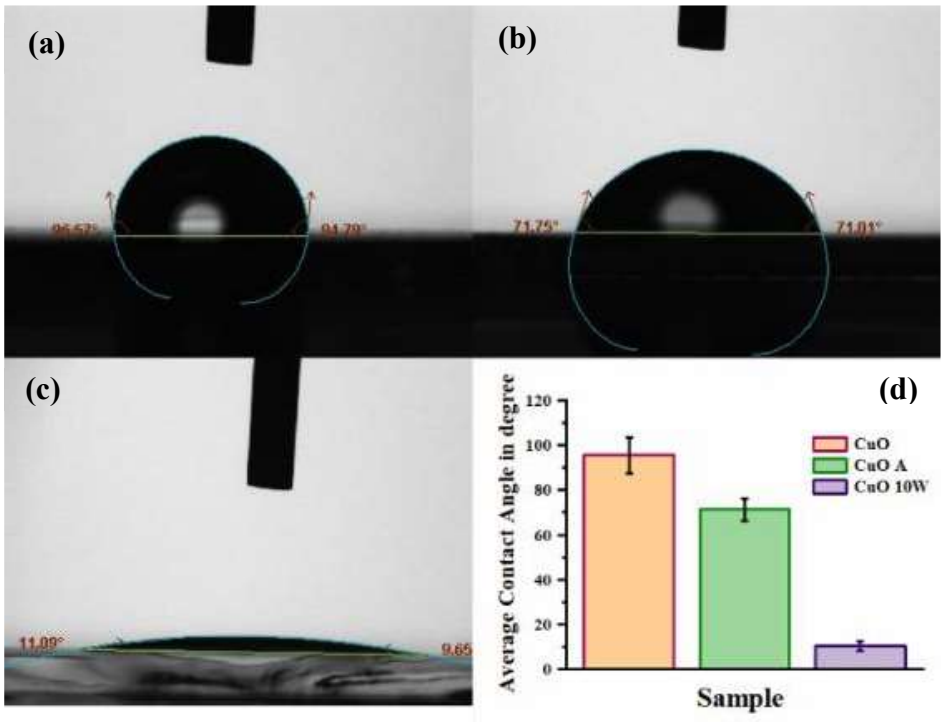


**Figure 1.** Water contact angle for (a) as deposited CuO (b) air-annealed CuO (A), (c) CuO annealed in presence of plasma (P) , (d) variation in contact angle for the three CuO surfaces.

One of the fundamental factors that influence the electrocatalytic activity is the surface wettability of the electrode.[47] During the process of water electrolysis, both oxygen evolution at anode and hydrogen evolution at cathode, are affected by the

wettability of electrodes. [48,49] As electrolyte-wetting of the electrodes is critical for faster redox electron transfer and evolution of gas during electrochemical reactions, it has been reported that a hydrophilic surface enhances the extracellular electron transfer rate between microbes and electrode in a microbial fuel cell assembly. [50] In a water electrolysis process, the cell voltage, E, is represented as:

$$E = E_0 + \eta_{anode} + \eta_{cathode} + iR \qquad (2)$$

Where, "$E_0$" is the theoretical thermodynamic term, "$\eta_{anode}, \eta_{cathode}$" stands for the overpotential values at anode and cathode, respectively, and "*iR*" represents the Ohmic resistance. [47] *iR* drop results from the interfacial contact resistance between electrode-electrolyte and gas bubbles during electrolysis. During oxygen evolution at the electrode, the nucleation and growth of oxygen bubbles is retarded for a hydrophilic surface due to lowered adhesion of the generated gas.[51] This faster mass transfer keeps the nucleation sites free for new bubbles to be produced in succession. Moreover, the lower coverage of gas molecules on the electrode reduces the surface contact resistance. In our case, the as deposited CuO demonstrated an average (CA) of ~ 95° while after annealing for 5 mins, the CA value dropped to ~ 71° as can be observed from Figure 1. This could be due to the reduction in surface roughness after annealing. For CuO annealed in plasma atmosphere, the CA dropped drastically to ~10°, thus, turning the surface super-hydrophilic. This could lead to a significant drop in charge transfer resistance in the impedance spectra. Surface hydroxylation is one of the effective routes to enhance the hydrophilicity of the electrode material/surface. [52] Hydroxyl radicals induce polarity to the surface and enhances the hydrogen bonding between electrode and electrolyte. As already mentioned, plasma jets are an abundant source of hydroxyl and oxygen radicals, seen in Figure 2(d). The exposure to plasma acted as the hydrophilic treatment resulting in the increase of electrodes surface energy.

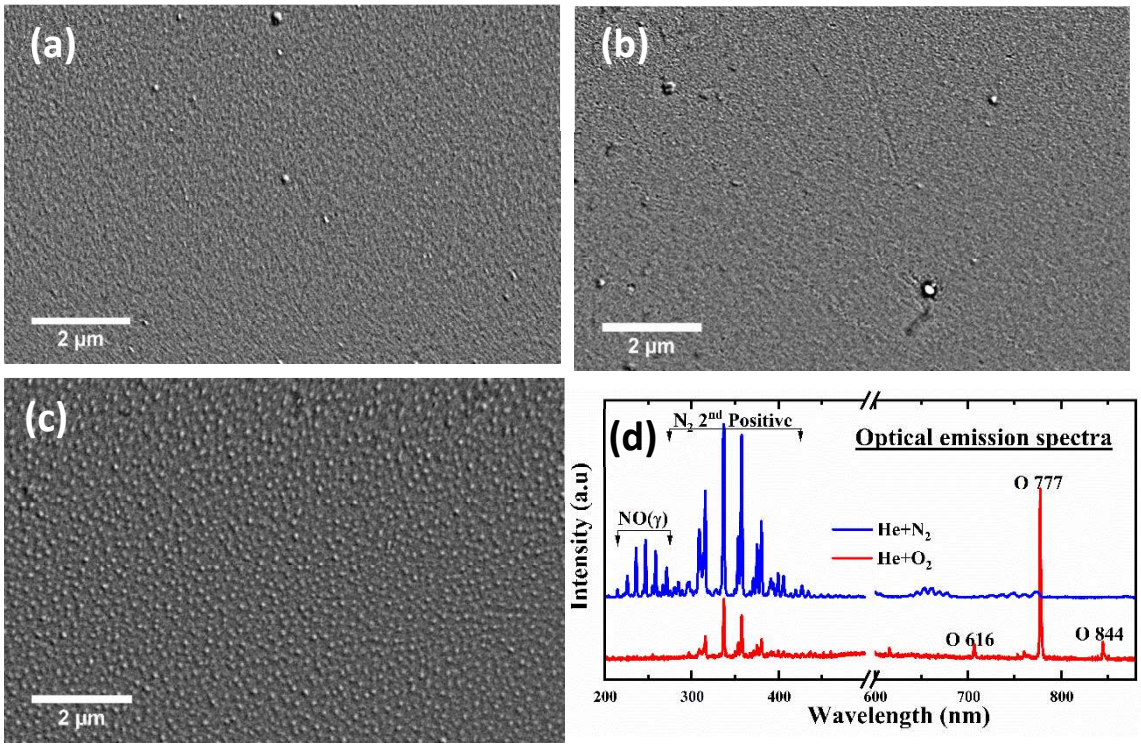


**Figure 2.** Scanning electron microscope image of (a) CuO ,(b) CuO(A) , (c) CuO(P) thin films, (d) optical emission spectra corresponding to $He+O_2$ and $He+N_2$ plasma jet.

Electron micrographs of the as deposited CuO films reveal a very smooth surface composed of nano-sized crystallites. Thermally annealed CuO [Figure 2(b)] shows similar surface morphology to the as-deposited CuO thin film [Figure 2(a)]. Our previous study showed that grain boundaries become prominent when annealed at 550 ºC.[17] Annealing in the plasma environment increases the surface roughness and noticeable patterns are formed on the surface of the film [Figure 2(c)]. Increasing the surface area is one of the potent routes for enhancing the electrocatalytic and phtocatalytic activity of the catalyst. By introducing nanoscale surface features the active area of the catalyst could be increased, inturn enhancing the catalytic activity. [53] The distinctive surface features observed in the plasma functionalised film could be resulting from the the strain developed during grain boundary sliding. Interestingly, Studies

have shown that formation of patterned and rough surfaces increases the water contact angle.[54–56] However in contract to these reports, the patterned CuO surface is superhydrophillic in nature. This could mostly be due to formation of surface oxygen or hydroxyl gorups that promote water contact through hydrogen bonding. The evolution of microstructure is initiated when the temperature is high enough to overcome the activation energy of grain boundary motion. From the electron micrograph for CuO(A) it is clear that in the described timescale and at 375 ºC there is no observable microstrutural evolution [Figure 2(b)]. However,plasma accelerates the process of grain growth by decreasing the interfacial energy. Plasmas are known to increase entropy during lattice transformation by inducing deformation and defects. [57] Figure 2(d) shows the optical emission spectra for $He+O_2$ And $He+N_2$ plasma jets. The emission spectra reveal a variety of emission peaks within the wavelength range of 200 nm to 880 nm. APPJ's are rich in neutral and charged species and radicals. Of these oxygen radicals are highly active and can diffuse into the surface resulting in unusual surface morphologies.[57] Presence of these surface features in CuO(P) could play a critical role in enhancing the catalytic properties of this electrode material.

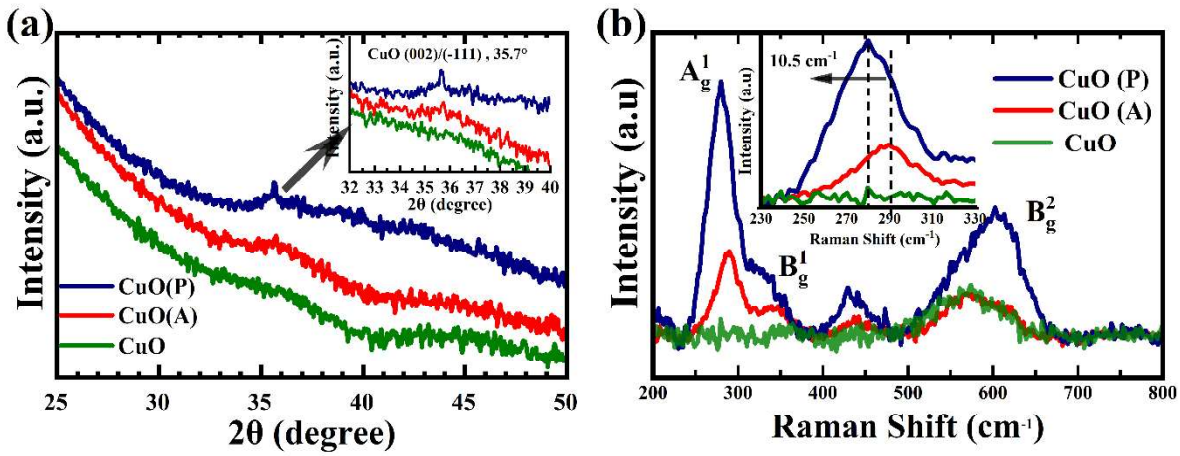


**Figure 3. (**a) X-ray diffractogram and (b) Raman spectra comparing CuO, CuO(A), and CuO(P) thin films.

The structural properties of the three electrode materials were studied using X-ray diffraction and Raman spectroscopy. No distinctive peak could be observed for as-deposited CuO . This is due to the lack of long-range order in the lattice of as-deposited CuO thin films due to the lack of long-range order in the lattice [Figure 3(a)]. Our previous study showed that post synthesis annealing is essential to enhance the crystallinity of the sputtered films.[17] The diffractogram for CuO(A) was found to be very similar to CuO, showing 5 mins of thermal annealing is not sufficient to induce crystallinity in the lattice. [Figure 3(a)] However, for CuO(P) the diffractogram showed for CuO(P),shows the presence of two prominent peaks between 20-25 °. The peak at 23.4º could be assigned to (021) lattice of $Cu(OH)_2$.[58] CuO(P) showed enhanced crystallinity with grain growth along the (002)/(-111) lattice orientation at 35.7º as shown in the inset of Figure 3(a). This observation also confirms that plasma accelerates the evolution of microstructure. The preferential growth along (002)/(-111) could be due to the low binding energy of these low index crystal planes. At high temperature, thermal energy provides the required energy to make the adatoms mobile, thus, reaching the favoured lattice positions.[17] The increase in entropy from the presence of plasma enhances the mobility of these adatoms. Raman spectroscopy is a complementary technique to identify the structural disorder, defects, and crystallinity of thin film. Full width at half maxima (FWHM) of the Raman peaks can be used as a measure of the crystallinity of nanostructure films. For nanometre sized system, phonon confinement plays a crucial role. This phenomenon leads to the apparent shift and broadening of the Raman peak. The Raman spectra for CuO (red line) shows a broad feature at 570 $cm^{-1}$. [Figure 3(b)]. The absence of any other phonon mode proves the absence of any long-range order or crystallinity in the as -synthesised thin films. After thermal treatment, characteristic modes of CuO could be observed in the Raman Spectra. For crystalline CuO , distinct peaks are observed around 290, 340 and 620 $cm^{-1}$ corresponding to A1g , B1g and B2g phonon modes respectively. [31] In Raman spectra, peaks become intense

and show blue shift with increase in grain size whereas red shift is associated with lattice strain. Both of these phenomena could be observed in the Raman spectra for CuO(A) and CuO(P).) [Figure 3(b)]. The increase in intensity for A1g and B2g modes with plasma functionalisation relates to the larger crystallite size for CuO(P). Moreover, the B2g mode shifts to higher wave number for CuO(P) indicating the order in lattice. Interestingly, the A1g mode [inset of Figure 3(b)] red shifts by 10 $cm^{-1}$ , revealing that plasma functionalisation introduces strain in the lattice. This could be due to lattice expansion or anisotropy caused by oxygen -rich environment in the plasma. Findings from XRD and RAMAN analysis confirm that plasmas can introduce degeneracy in morphology and crystal structure which could prove advantageous for catalytic applications.

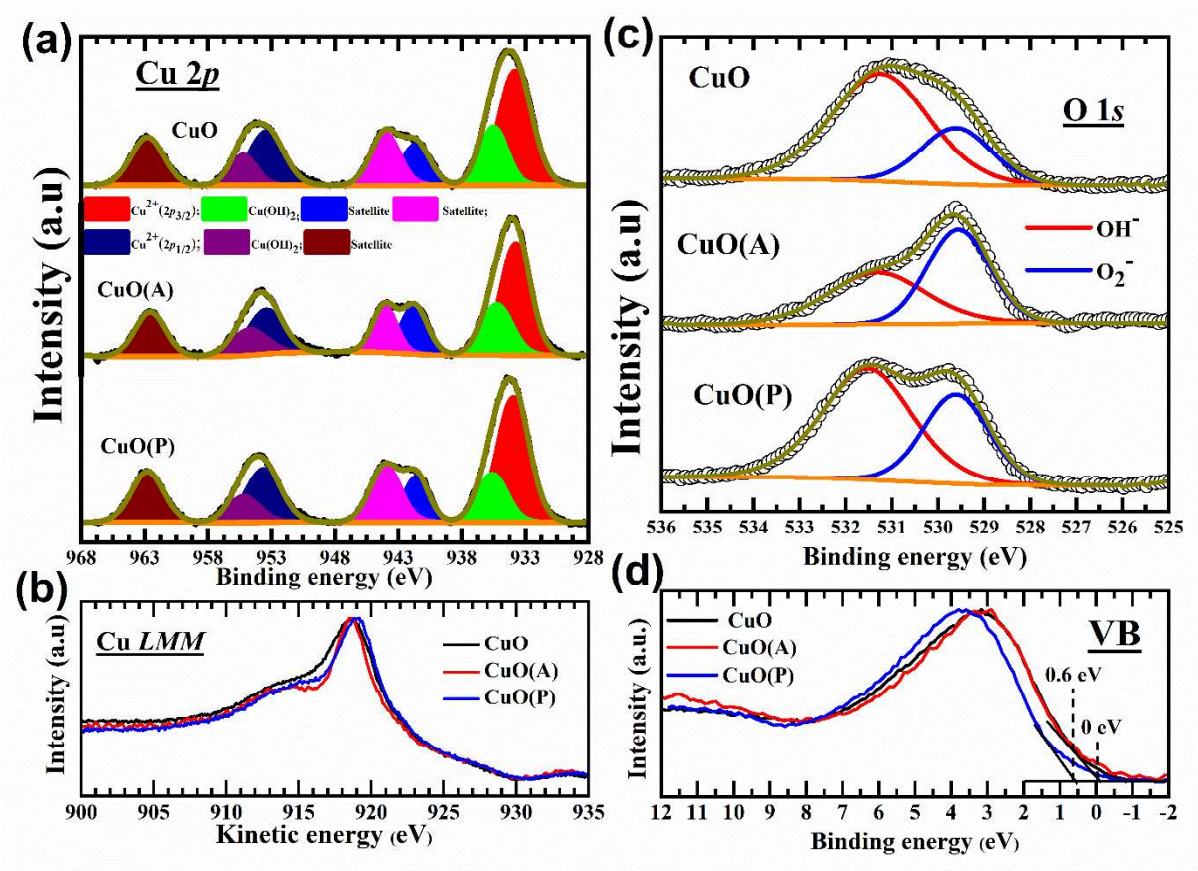


**Figure 4.** X-ray photoelectron spectra of (a) Cu 2*p*, (b) Cu LMM, (c) O1*s* and (d) valence band of as-prepared, furnace-annealed and 10 W $He+O_2$ plasma treated copper oxide films.

X-ray photoelectron spectroscopy (XPS) was used to understand the variation in surface chemical and electronic properties of CuO, CuO(A) and CuO(P) thin films. APPJ consists of abundant oxygen, hydroxyl radicals and excited molecules that can induce disorder in the chemical, electronic and crystal structure of the surface being treated XPS is a highly surface-sensitive technique with the signal originating from a thin layer at the surface (<5 nm). Any changes in the surface electronic and chemical environment would induce shifts in the core and valence energy levels. Figure 4 shows the corresponding Cu2*p,* Cu Auger, O1*s* core level and valence band spectra of the copper oxide samples. Figure 4(a) shows the characteristic Cu2*p* core level spectra of the copper oxide films, characterized by a doublet feature at around 934.3 eV and 954.1 eV corresponding to Cu2$p_{3/2}$ and Cu2$p_{1/2}$ states, respectively, with a splitting of 19.8 eV. The Cu2*p* spectrum also shows a characteristic 'shake-up' satellite at 943.0 eV, which is ~8.7 eV separated from the primary Cu2$p_{3/2}$ peak. Satellites are typical for copper oxides and occur due to multi-electron transitions between unoccupied Cu3*d* orbitals and O2*p* orbitals and confirm the $Cu^{2+}$ state of the films. [59,60] For all samples , the presence of a series of shake-up satellite peaks observed at 941.5 ± 0.1 eV, 944.1± 0.1 eV and 962.6 ± 0.2 eV can be assigned to the unfilled Cu3$d^9$ shell and corroborates to the +2 oxidation state of Cu . [59] Figure 4(a) illustrates the Cu 2$p_{3/2}$ spectrum of CuO, CuO(A) and CuO(P) could be deconvoluted into two components around 933.7 ± 0.1 eV and 935.4 ± 0.1 eV to gain deeper understanding of the oxidation state of copper under different treatment conditions. The lower binding energy (BE) component for all the samples at ~933.7 eV was assigned to $Cu^{2+}$. [61] The higher energy component at ~935.4 eV is believed to have a contribution from $Cu(OH)_2$ as well as the other species adsorbed on the copper oxide films. This plasma-surface interaction to produce surface adsorbed species would validate the ~0.7 eV shift in the BE position of $Cu(OH)_2$

reported elsewhere in literature. [62,63] In addition, FWHM of the $Cu^{2+}$ $2p_{3/2}$ decreases from 3.1 eV for as-prepared samples to 2.7 eV for CuO (A) and 2.9 eV for CuO(P) This would suggest an enhancement in the crystallinity of the samples after heat treatment. The disordered structure of CuO(P) could have resulted in relatively higher FWHM with respect to CuO(A). The Cu$2p_{1/2}$ peak has also been fitted with two components at 953.2 and 955.1 eV keeping the parameters same as the $2p_{3/2}$ state. The oxidation state of Cu was further probed by investigating the Cu LMM region using X-ray induced Auger electron spectroscopy (AES) as shown in Figure 4(b). A sharp peak is observed at about 918.7±0.1eV (kinetic energy) corresponding to the Cu *LMM* Auger feature. Observed reduction in FWHM of the Cu LMM feature of the CuO films signifies rearrangement of surface chemical structure upon heat and plasma treatment.

The O1*s* spectra of as-prepared CuO sample was deconvoluted into two components corresponding to the lattice oxygen and a broad component with contribution from hydroxyl groups and/or surface-adsorbed oxygen, at ~529.5 ± 0.1 eV and ~531.3 ± 0.2 eV, respectively, as shown in Figure 4(c). The peak positions of the different O1*s* components are within ± 0.2 eV of previously published reports.[62] The spectra of CuO(A) and CuO(P)shows significant variation in spectral feature. As Figure 4(c) illustrates, the lattice oxygen content of the films show an increase, both upon heat and plasma treatment, from 27.2% (as-deposited) to 53.4% (annealed) and 36.4% (plasma).This is proposed to result from the desorption of the hydroxyl groups from the surface upon thermal treatment along with crystallization of the lattice. In addition, a 0.2 eV reduction in the FWHM of the lattice oxygen also suggests the decrease in mixed ionic states of Cu at the surface of films. This enhancement in crystallinity of the samples post annealing can be corroborated from the reduction in the FWHM of the $Cu^{2+}$ main line as observed earlier. A considerable decrease in higher energy component

is observed for CuO(A), due to the temperature induced desorption of molecules. Interestingly, for CuO(P) this component presents a strong spectral signature along with a shift towards higher binding energy. Also, a 0.4 eV increase in FWHM of the higher BE component at ~531.3 eV of CuO(P) maybe assigned to the adsorption of different species from the APPJ which consists of abundant electronegative species including $NO_x$ and oxygen radicals ($O_2$, $\bullet O^{2-}$ or $\bullet O^-$). Exposure to plasma may result in the chemisorption of one or more of these species at the very surface of the films, thus resulting in shift of the electron cloud from the hydroxyl core. The positive shift in the O1*s* spectra maybe assigned to this charge separation. The valence band (VB) region of the samples was also probed as shown in Figure 4(d). Limited variation is observed in the line shape and position of the VB spectra of CuO and CuO(A) films. The Cu3*d* region is detectable around 3.0 eV below the Fermi level, as well as the O2*p* region, centred at around 5.0 eV. A significant shift of ~0.6 eV and enhancement in the partial density of states at ~ 5.0 eV is observed in the VB spectrum of CuO(P) films. This is most likely due to the enhanced contribution to the O2*p* states from the chemisorbed oxygen species or due to the quenching of lattice hydroxyl groups within the lattice. The 0.6 eV shift in the VB maxima (VBM) could be assigned to the formation of CuO(OH) due to the interaction of the $OH^-$ and other radical groups in the plasma with the CuO film. The increase in density of states (DOS) around 5.0 eV also signifies the addition of hydroxyl groups into the CuO lattice. The formation of additional features due to $OH^-$ groups can be corroborated from the O1*s* spectra (Figure 4c).

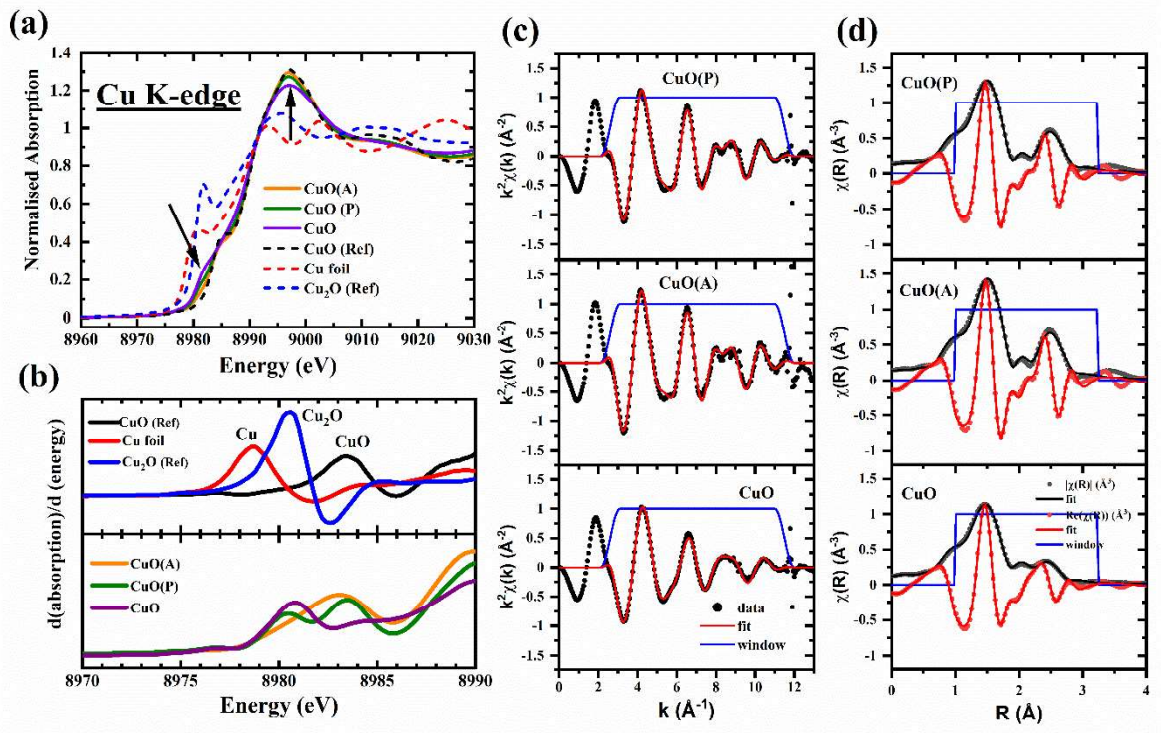


**Figure 5.** (a) Cu *K*-edge XANES spectra of CuO thin films. The spectra are compared with standard CuO, $Cu_2O$ and Cu samples. (b) first derivatives of the Cu *K*-edge spectra, (c) EXAFS oscillations in k- space, (d) Fourier transforms (FTs) of the EXAFS oscillations.

To get insight into the variation in electronic and local structural properties with plasma functionalisation of the CuO catalysts, Cu *K*-edge X-ray absorption fine structure (XAFS) spectra including X-ray absorption near-edge structure (XANES) and extended X-ray absorption fine structure (EXAFS) was aquired. In contrast to XPS, XAFS probes the local electronic and structural details of a specific atomic species in the material.[64] Careful analysis of the EXAFS spectra provides information about the short-range order, atomic distances and coordination number with high accuracy and sensitivity. Figure 5(a) shows the normalized Cu *K*-edge spectra of the CuO catalysts. For comparison, a CuO reference has been presented simultaneously. The pre-edge region consists of three distinctive features: an intense peak at 8997.0 eV, a shakedown feature between 8980-8990 eV and a weak absorption pre-edge feature at 8977.0 eV. The intense edge feature corresponds to the dipole-allowed

transitions from $1s \rightarrow 4p$ (continuum) states. The weak pre-edge peak at 8977.0 eV results from the quadarpule allowed $1s \rightarrow 3d$ transitions. This feature is a signature of the $Cu^{2+}$ state stemming from its $3d^9$ configuration. For $Cu^{1+}$ because of the closed shell $d^{10}$ configuration, these $1s \rightarrow 3d$ transitions cannot exist. Although, this $1s \rightarrow 3d$ transition is forbidden under the dipole selection rules, it could be detected due to the $3d + 4p$ orbital mixing along with vibronic and direct quadrupole coupling. Here, the quadrapole transitions can be neglected due to the much lower transition probability with respect to the dipole transitions. The shake-down feature corresponds to $1s \rightarrow 4p_z$ transitions concurrent with ligand to metal charge transfer character. For $Cu^{2+}$ it can be observed as an intense peak at ~8986 eV and shifts to lower energies for $Cu^0$ (8980 eV ) and $Cu^{1+}$ (8982 eV).[65] It is to be noted that the features corrresponding to $Cu^0$ , but a small contribution from $Cu^{1+}$ could not be disregraded aswell. However, there are signatures in the XANES region for both $Cu^{1+}$ and $Cu^{2+}$, this could be due to the distortion in the lattice symmetry of CuO. First dervative of the XANES spectra have been shown to make the pre-edge features more distinctive. Figure 5(b) indicates that there is significant variation in the local environment of copper between the samples. The as-deposited is partially in the $Cu_2O$ type structure, as noted by the intensity of the feature at 8982 eV. After annealing for 5 mins, the structure reforms towards the characteristic CuO symmetry. Interestingly, the plasma functionalised sample showed a mixed phase of the $Cu_2O$-type and CuO-type structures, plasma treatment appears to partially restore some $Cu^{1+}$ species. The thin film annealed in the plasma atmosphere attains a superlattice structure due to the pseudo presence of $Cu_2O$ like symmetry.[66] This could be due to the increase in entropy caused by the various energetic species in the plasma. Another reason could be the formation of bonds between $Cu^{2+}$ and $OH^-$ groups, which causes the formation of a distorted octahedron around $Cu^{2+}$ during the crystal growth. This observation can be corroborated to the distortion in thelattice in the form of red

shift of the A1g mode in Raman spectra. XRD data also supports the formation of crystalline $Cu(OH)_2$ along with the growth of CuO grains.

To further understand the strutural evolution, the post-edge features of the absoprtion spectra were analysed. Figure 5 (c,d) shows the EXAFS spectra of the CuO catalysts in *k*-space and the Fourier transformed (FT) EXAFS spectra in *R*-space, respectively. For the *k*-space transformation the data range was taken from 2 to 12 $Å^{-1}$ and fitted in the *R*-space in the range of 1−3.2 Å to obtain the structural parameters. In the (unphase corrected) *R-space* spectra, the peak between 1−2 Å arises from scattering due the Cu and first coordinate O while the second peak at 2-3 Å is associated with the Cu-Cu coordination.[65] Table 1 presents the calculated shell parameters *i.e.* bond-distance (*R*), coordination number (*N*) and Debye–Waller factor ($\sigma^2$). From the XANES analysis, the chemical environment of the catalysts were found to be similar to CuO. Thus, we considered CuO as the primary model for fitting of all the catalysts.The FT oscillations reveals the difference in structural evolution of CuO annealed in two different environments. Though the first $Cu^{2+}$-$O^{2+}$ (~1.9 Å) and second $Cu^{2+}$-$Cu^{2+}$ (~2.9 Å) shells have similar structural parameters, the coordination numbers are distinctly different between CuO(A) and CuO(P).)[66] The slight decrease in the Cu-O and Cu-Cu coordination numbers suggests increased deformation in the local atomic arrangement of CuO(P) with respect to CuO(A).[67]

| Sample | Scattering Path | Radial Distance (Å) | Coordination Number | Debye Waller Factor ($Å^2$) |
|---|---|---|---|---|
| CuO | Cu-O | 1.93 ± 0.02 | 3.4 ± 0.3 | 0.005 ± 0.002 |
| | Cu-O | 2.78 ± 0.04 | 0.8 ± 0.2 | 0.005 ± 0.002 |
| | Cu-Cu | 2.86 ± 0.04 | 1.6 ± 0.2 | 0.010* |
| CuO(A) | Cu-O | 1.95 ± 0.02 | 3.8 ± 0.3 | 0.003 ± 0.001 |
| | Cu-O | 2.82 ± 0.02 | 1.1 ± 0.2 | 0.003 ± 0.001 |
| | Cu-Cu | 2.92 ± 0.04 | 3.0 ± 0.4 | 0.010* |
| CuO(P) | Cu-O | 1.94 ± 0.02 | 3.6 ± 0.3 | 0.004 ± 0.002 |
| | Cu-O | 2.82 ± 0.02 | 1.0 ± 0.2 | 0.004 ± 0.002 |
| | Cu-Cu | 2.91 ± 0.04 | 2.7 ± 0.3 | 0.010* |

**Table 1.** Structural Parameters of CuO, CuO(A) and CuO(P) determined from EXAFS measurement

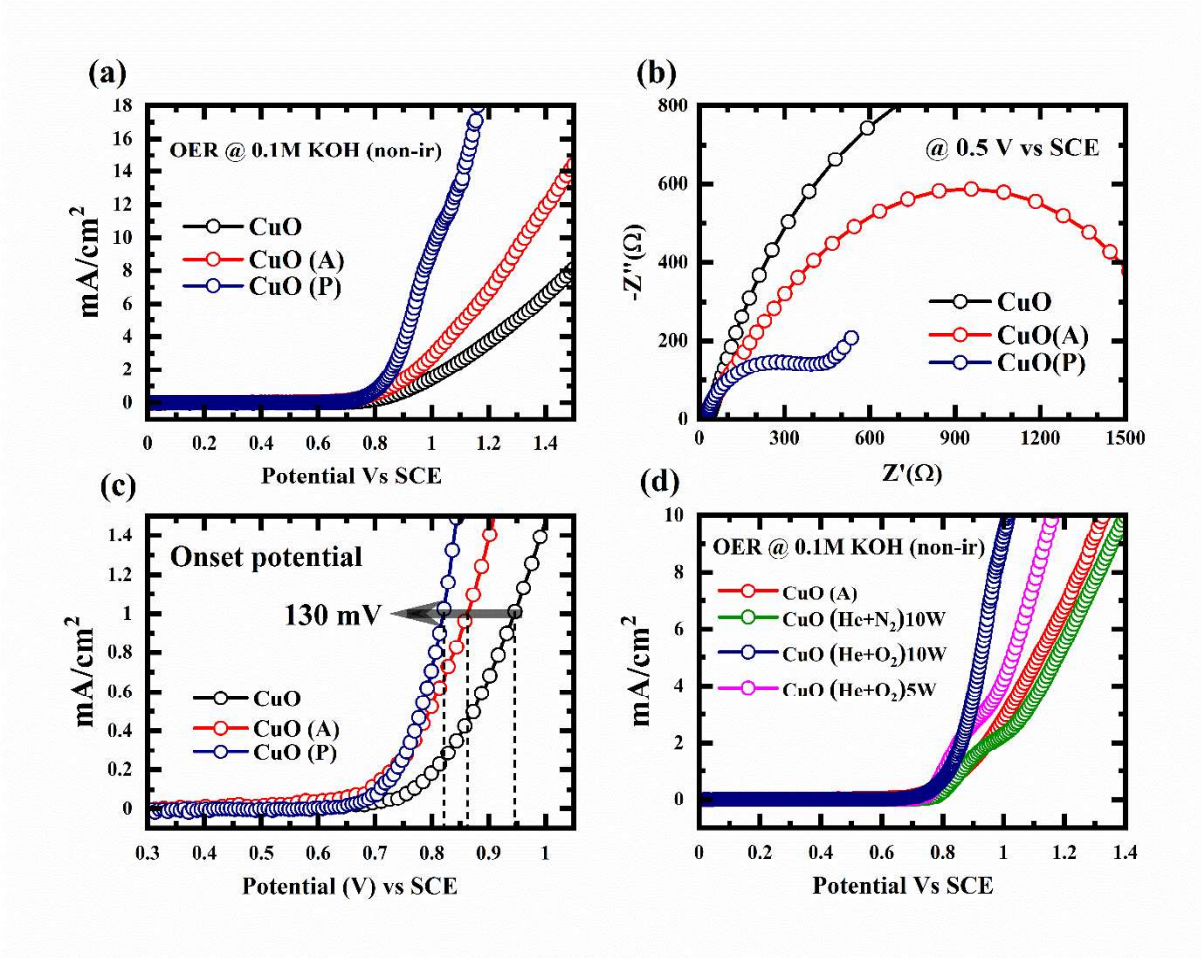


**Figure 6**. (a) Linear sweep voltammetry plots for CuO ,CuO(A) and CuO(P) in 0.1M KOH taken at a scan rate of 1 $mVs^{-1}$ (b) electrochemical impedance spectra for CuO ,CuO(A) and CuO(P) at 0.5V vs SCE, (C) Expanded view of the LSV plot to show the difference in onset potential between the three electrodes (d) comparison between the OER activity CuO(A) and CuO treated at different plasma conditions KOH taken at a scan rate of 1 $mVs^{-1}$.

The catalytic activities of the as-deposited, annealed and plasma functionalised CuO films towards OER were investigated using linear sweep voltammetry (LSV) at a scan rate of 1 mV $s^{-1}$ in 0.1 M KOH (pH 13) electrolyte. Electrocatalytic properties were measured in a three-electrode configuration with Pt wire as the counter electrode and SCE (4M KCL) as the reference electrode. Polarizations data was acquired without compensating for the *iR* drop, which appears at the solid-electrolyte interface. Current density of the electrode was

determined from the LSV curves after dividing by the electrode surface area. All the CuO electrodes showed catalytic activity towards water oxidation as shown in Figure 6(a). With an anodic scan from 0 to 1.5 V vs SCE, gas bubbles were discernible on the surface of the CuO electrodes from ~0.9 V. LSV curves revealed that the activity towards water oxidation clearly improved after annealing and plasma functionalisation with plasma functionalised electrodes showing the best performance. The plasma functionalized electrode achieved a catalytic current density of 10 mA $cm^{-2}$ which was more than 3 times that in case of annealed CuO electrode (3 mA $cm^{-2}$ ) at 1 V vs SCE, while the as deposited CuO electrode could achieve a meagre 1.4 mA $cm^{-2}$ at same potential. Figure 6(b) shows the Nyquist plots for the electrodes taken at 0.5V vs SCE. The semicircle feature of Nyquist plot results from the redox charge transfer process at the electrode-electrolyte interface. The measured diameter of this semicircle represents the charge transfer resistance (Rct). Rct dropped drastically after high temperature processing of the electrodes, from 3.5 kΩ for CuO to 2 kΩ for CuO(A) before reducing further to 0.6 kΩ for CuO(P) . This proves that with plasma functionalisation results in dramatic enhancement in the redox activity of the electrodes substantially. Moreover, the onset potential could be reduced by 130 mV for 1 mA $cm^{-2}$ with plasma functionalisation, as shown in Figure 6(c). The enhanced activity for the plasma functionalised electrodes could be attributed to the formation of nanoscale surface features, increased crystallinity, as well as the electrostatically bonded surface hydroxyl groups. Moreover, the drop-in water contact angle as shown in Figure 1 is predicted to be a critical factor. During OER, the water oxidation is initiated via the formation of CuOOH. The dissociation of CuOOH , results in evolution of $O_2$ and the catalyst is recovered. As observed in O1*s* spectra of CuO(P), the electrode surface is rich in $OH^-$. However, the pritine CuO surface also showed adundant $OH^-$ on the surface, which are either loosely bound or adsorbed. These adsorbed species did not influence the catalytic activity. Hence, the presence of CuOOH on the surface would make the process of water oxidation more

energy efficient, resulting in lower onset potentials and faster redox kinetics as seen for CuO(P). To validate this theory, the CuO films were treated with different plasma conditions. One sample was exposed to $He+O_2$ plasma but at 5W power, whilst a second sample was treated with $He+N_2$ plasma operated at 10 watts. The presence of $N_2$ quenches the formation of oxygen and hydroxyl radicals [as shown in Figure 2(d)] while at 5 W, radicals are present in a lower concentration in the plasma. It can be seen from Figure 6(d) that the catalytic activity is substially reduced in case of $He+N_2$ plasma functionalised electrodes, whereas samples at 5W still show enhanced activity with respect to the annealed sample. The electrochemical studies present an important breakthrough in enhancing the activity of electroctalysts by pre-hydroxilation through plasma functionalisation.

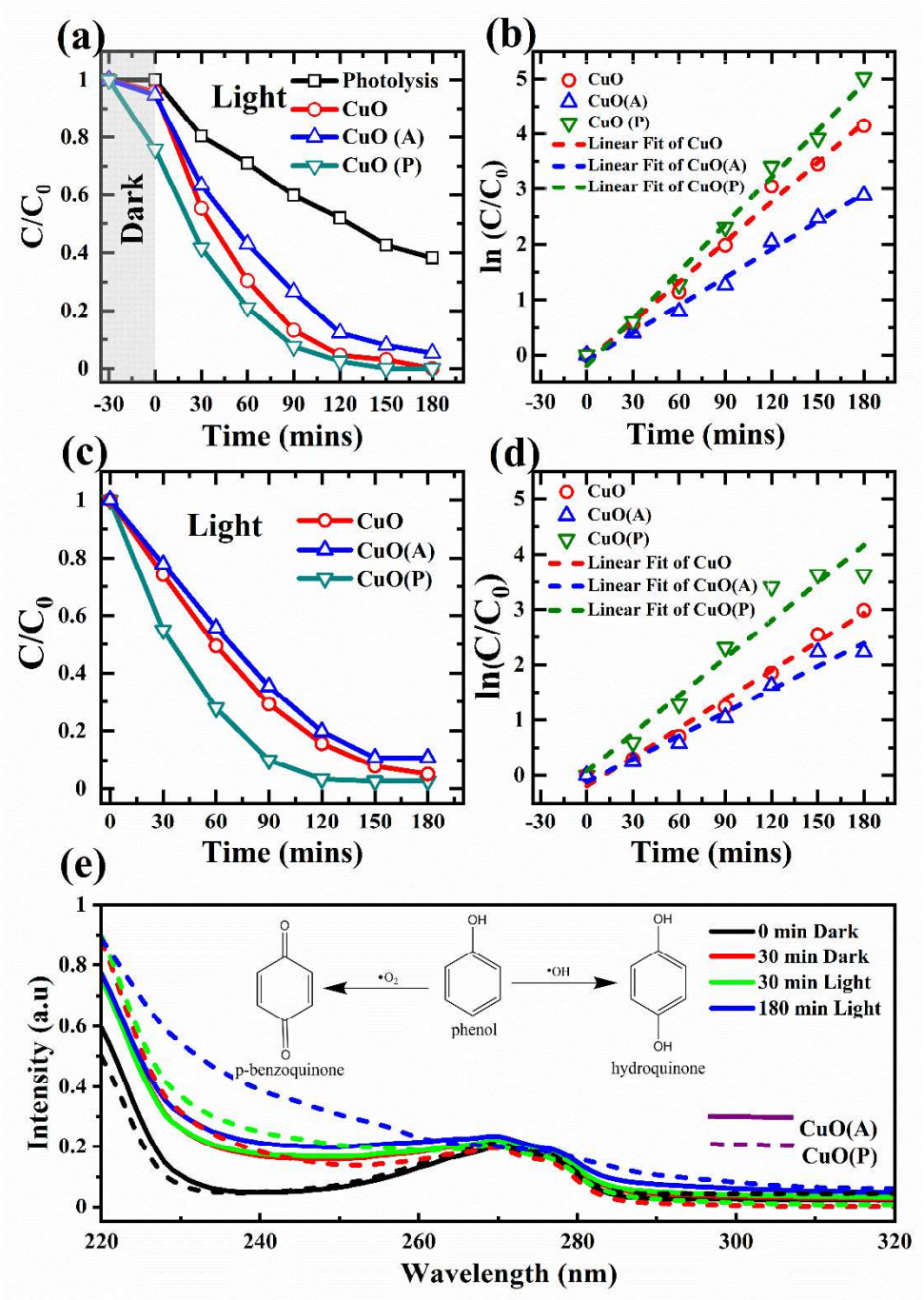


**Figure 7**: (a) Dark mode adsorption and light mode photocatalytic degradation of MB by batch-I samples of CuO, CuO(A) and CuO(P); (b) Photocatalytic degradation kinetics of MB by batch-I samples of CuO, CuO(A) and CuO(P); (c) Light mode photocatalytic degradation of MB by batch-II samples of CuO, CuO(A) and CuO(P); (d) Photocatalytic degradation kinetics of MB by batch-II samples of CuO, CuO(A) and CuO(P); (e) UV-Vis absorption spectra depicting photocatalytic degradation of phenol at different time intervals. CuO thin films kept in 30 minutes dark(D) to reach equilibrium before exposure to simulated sunlight (L).

CuO has been widely used as photocatalyst for degradation of organic pollutants. In this section, we intend to demonstrate that the activity of CuO photocatalysts could be boosted with plasma functionalisation and understand the possible underlying mechanism. The photocatalytic activity of CuO thin films (as-deposited, annealed, and plasma-treated) was investigated by using them to degrade Methylene Blue under visible light matching solar spectra, and the performance is compared in Figure 7. It is to be noted, all the photodegradation measurements were carried out in the presence of $H_2O_2$. Hydrogen peroxide ($H_2O_2$) accelerates the photocatalytic activity of CuO photocatalysts by acting as an electron scavenger and in releasing high energy •OH species which degrades the organic dye molecules. Two batches of CuO, CuO(A), and CuO(P) were used to study their photocatalytic activity. In batch-I [Figure 7(a))], the photocatalyst thin films were immersed in the MB dye solution and stored in dark condition for 30 minutes at room temperature to attain the adsorption/desorption equilibrium. After the dark mode, the photocatalysts immersed in dye solution were irradiated with visible light. But in batch-II [Figure 7(c))], the photo-degradation test was undertaken directly under light mode without involving dark mode adsorption/desorption equilibrium. Figure 7(b) and 7(d) show the degradation kinetics of MB for the CuO films, and the rate constant (k) of degradation for each is obtained by calculating the slope of the plot $\ln(C/C_0)$ vs. time where $C_0$ and C represent the concentrations of MB before and after light irradiation, respectively. In both the batches, the photocatalysts have the following order of photo-degradation efficiency and kinetic rate constant (k): CuO(P) > CuO > CuO(A).

It is reported that amorphous CuO has larger bandgap (2.3 eV) compared to annealed crystalline CuO (1.7 eV), which might favour the optical absorption property of visible spectra in amorphous CuO. [68] XRD and Raman results (Figure 3) indicate to the amorphous nature of the as-deposited CuO. Annealing at 375 °C (5 min), improves the crystallinity of the CuO(A). Hence, the as-deposited CuO shows a higher MB degradation efficiency and rate

constant (k) compared to CuO(A). However, (Figure 2) of as-deposited CuO and CuO(A) does not show any characteristic difference in morphology. SEM image (Figure 2) of CuO(P) showed the formation of nanodots on the surface. XRD and Raman spectra show further improvement in crystallinity for CuO(P) sample compared to CuO(A). Increase in crystallinity and grain size is one of the key factors which enhances the photocurrent generation or photocatalytic degradation in CuO.[17] Also, these nanostructures could act as plasmonic centres to trap the light and enhance the optical absorption. [69] Thus, CuO(P) with higher surface area shows the degradation rate (k) of 0.0283 $min^{-1}$ (batch-I) and 0.0227 $min^{-1}$ (batch-II) which is higher than CuO (0.0173 $min^{-1}$) and CuO(A) (0.0139 $min^{-1}$). The average degradation efficiency of CuO(P) photocatalysts from the two batches was around 93% after 90 minutes of visible light irradiation, which is higher than CuO (80%) and CuO(A) (70%). Table 2. Compare the activity of CuO(P) with respect to recently published data. This also proves the effectiveness of the proposed process; a higher degradation rate could be achieved with just 5 minutes of plasma treatment. Adsorption is another key factor that accelerates the degradation and plays a major role in the photocatalysis process. An increase in surface area and enhanced hydrophilic nature of CuO(P) promotes surface adsorption of dye molecules. The surface hydroxyl groups on CuO(P) surface, changes the surface potential to negative, which in turn shows greater adsorption affinity towards cationic MB dye molecules.[70] Upon solar light irradiation, the photo-excited holes ($h^+$) from the CuO(P) photocatalyst are captured by surface hydroxyl groups and then oxidize the organic dye molecules, which are adsorbed on the photocatalyst surface [equation 2]. The trapped holes within the hydroxyl groups also activates the water oxidation process to release high energy hydroxyl radicals, which further degrades the organic dye molecules in the aqueous medium [equation 3a and 3b]. [68]

$$h^+ + \text{organic pollutant} \rightarrow \text{organic pollutant degradation} \quad (3)$$

$$h^+ + H_2O \rightarrow \bullet OH + H^+ \quad (3a)$$

$$\bullet OH + \text{organic pollutant} \rightarrow \text{organic pollutant degradation} \qquad (3b)$$

Methylene Blue is used here as the model pollutant because its concentration can be easily monitored using a UV-Vis Spectroscopy. However, as MB absorbs light in the visible range the influence of this photo-absorption cannot be excluded while evaluating the real photocatalytic activity of CuO thin film photocatalyst. To address this issue, we studied the photocatalytic degradation of phenol, which absorbs in the UV region around 270 nm.[33] Phenol is routinely found in industrial wastewaters, mostly chemical and petrochemical industries. [71] Figure 7(e) shows the UV-Vis absorption spectra of phenol taken at different intervals of time. The spectral features show drastic changes when CuO(P) is used as the photocatalyst. During photo degradation, phenol changes to p-benzoquinone (~240 nm) by the superoxide ($\bullet O_2^-$) radical and hydroquinone (~ 240 nm) by the hydroxyl radicals (•OH) as shown in the inset of Figure 7(e).[33] Hydroquinone and benzoquinone represent the first step in oxidative degradation of phenol. Previous reports have suggested that, these entities degrade further via ring opening reactions. [71] The spontaneous decay of $H_2O_2$ to $\bullet O_2^-$ led to the formation of benzoquinone even in the dark conditions, here $H_2O_2$ is used as the hole scavenger. Comparing the UV-Vis spectra after180 mins of light, plasma treated CuO shows faster oxidative decay of phenol with respect to annealed CuO. Mainly due to the faster photo-induced charge transfer accelerates the proposed reactions at the catalyst surface. These photo-generated charge carriers react with $H_2O_2$ producing hydroxyl and superoxide radicals, which breakdown phenol via multi step ring opening reactions. The results resented here proves the efficacy of CuO(P) towards photodegradation of a range of organic pollutants. It is understood that the formation of surface nanodots and surface hydroxyl groups on CuO(P) are two main aspects that determine both adsorption and photocatalytic degradation of MB represented schematically in Figure 8.

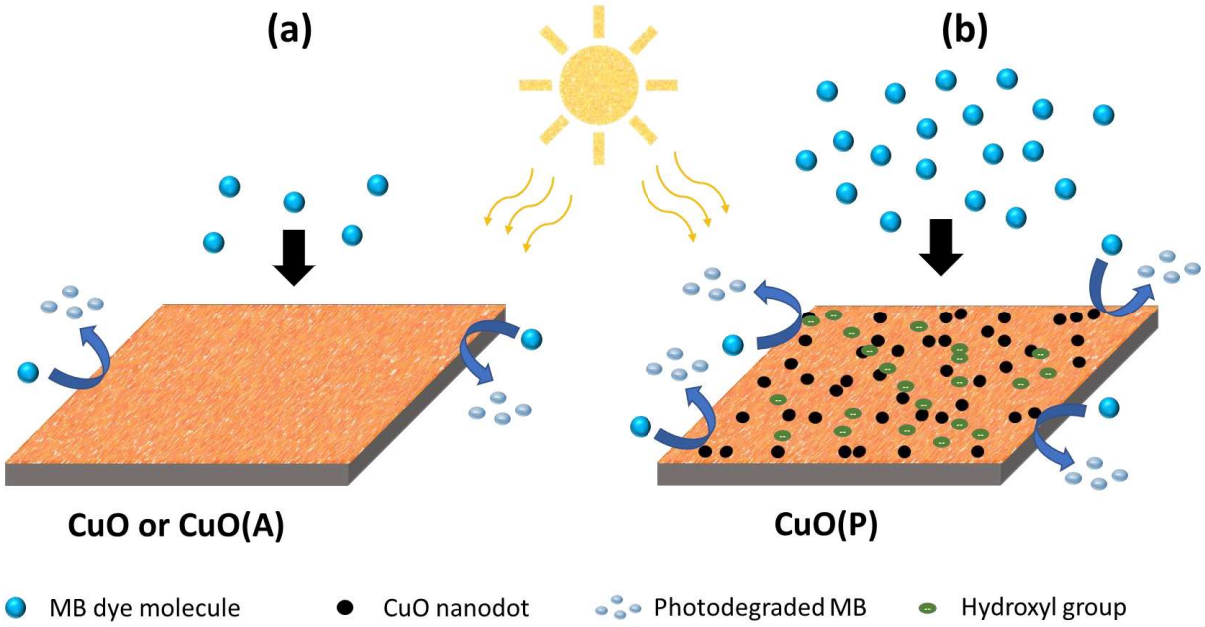


**Figure 8:** (a) Schematic illustration of CuO (or) CuO(A) with no characteristic surface morphology showing low MB dye adsorption and photocatalytic degradation; (b) CuO(P) with surface nanodots showing enhanced MB dye adsorption and enhanced photo degradation.

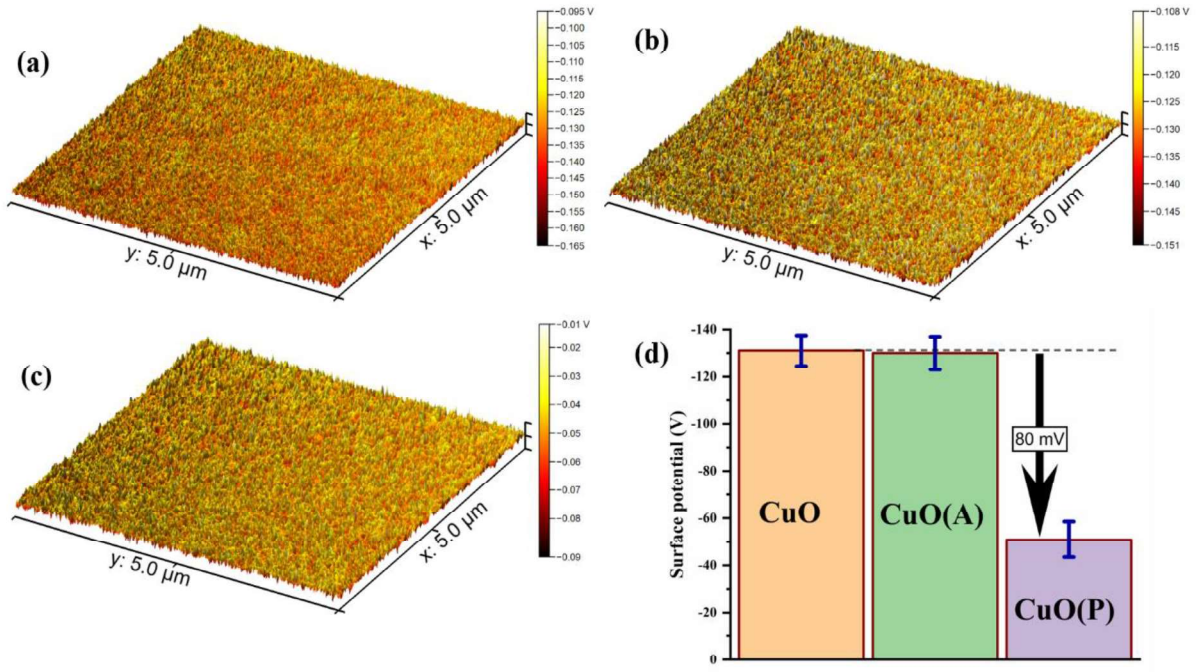


**Figure 9:** Surface potential map for (a) CuO , (b) CuO(A) (c) CuO(P) (d) Average surface potential value for the three CuO films. With plasma functionalisation the work function dropped by 80mV.

To further investigate the enhanced photocatalytic activity after plasma functionalisation Scanning Kelvin probe microscopy (SKPM) was carried out on these CuO thin films. In SKPM, a conducting tip with an applied bias is made to raster the sample surface and the feedback loop detects the surface potential (SP) as the difference in work function between the tip and the sample surface, i.e. $SP = \Phi_{Tip} - \Phi_{Sample}$.[30] Hence the surface potential value can indicate toward the relative increase or decrease in work function of the sample being measured. It has been reported, that work function of the electrode material influence the electron and proton transfer at the double layer region eventually effecting the rate of catalysis.[72] In our case a considerable drop by 80 mV in surface potential is observed with plasma functionalisation. This could be due to the formation of crystalline hydroxide. The presence of OH group lowers the energy level of the unoccupied states. The drop is also

supported by the 0.6 eV shift towards higher BE the in the valence band emanating form the increased density of O 2*p* states. This also indicates that, with plasma functionalisation the Fermi level is positively shifted towards the water redox potential favouring the electron transfer processes require for catalysis. The defects in the crystal structure as seen in EXAFS can introduce additional states near the unoccupied region causing the shift of the Fermi level. Also the large space charge region caused by the surface polar groups significantly enhances the electron-hole separation efficiency which in turn results in higher photocatalytic activity of the CuO. [73]

| **Sample** | **Method of synthesis / sample surface area** | **Dye molecule concentration / volume** | **Light Source / Degradation time / Degradation Rate/ Degradation efficiency** | **Ref** |
|---|---|---|---|---|
| CuO | RF Sputtering (300W, 300°C) 150 $mm^2$ | MB (10mg/L) 20 mL | Xenon arc lamp (AM1.5G, 150W), 2.5h, K= 0.03 $min^{-1}$, 99% | [74] |
| CuO | RF sputtering, 937.5 $mm^2$ | MB (10mg/L) 70 mL | Tungsten lamp (150W), 3h, 74.3% | [75] |
| CuO | RF sputtering (200W) | MB (10mg/L) 100 mL | Tungsten lamp (100W), 3h, K= 0.008 $min^{-1}$, 72% | [76] |
| CuO | RF Sputtering (200W) 150 $mm^2$ | MB (10mg/L) 20 mL | Xenon arc lamp (visible light, 300W), 5h, K≈0.012 $min^{-1}$, 78% | [77] |
| CuO | Thermal evaporation and Thermal annealing (400° C, 2h) | MB (5µM) 5 ml | Sunlight, 2.5h, K=0.015 $min^{-1}$, 70% | [78] |
| Au-CuO | Thermal Evaporation | MB (5µM) 5 ml | Sunlight, 2.5h, K = 0.021 $min^{-1}$, 72.3% | [79] |
| Ag-CuO | DC/RF magnetron sputtering | MB (10mg/L) 100ml | Sunlight, 3h, K = 0.010 $min^{-1}$, 85% | [80] |
| CuO | Electrodeposition and Thermal annealing (400° C, 2h) 100 $mm^2$ | MB (5µM), 5 ml | Sunlight, 1.5h, K = 0.025 $min^{-1}$, 91% | [81] |

| | | | | |
|---|---|---|---|---|
| CuO (P) | RF sputtering and APPJ (10W, 375° C) 150 $mm^2$ | MB (10mg/L) 20 mL | Solar Spectrum (300W), 2h, K= 0.028 $min^{-1}$, 93% | Current work |

**Table 2:** Comparison between the dye degradation activity of CuO(P) with recently reported values.

## 4. Conclusion

The present study demonstrates an innovative route to enhance the catalytic properties of CuO thin films using a low power atmospheric pressure plasma jet. The process involves annealing and simultaneously treating the CuO films with a helium-oxygen plasma jet. CuO films functionalized with APPJ demonstrated significantly higher electrocatalytic oxygen evolution and photocatalytic dye degradation activities. XRD and RAMAN studies revealed that plasma accelerated the crystallization of CuO domains and induced high degree of strain in the lattice. XANES and EXAFS techniques were applied to probe the local electronic/atomic structure of the CuO thin films. The spectral features revealed that for CuO(P) the atomic structure deviated from typical CuO structure. Additionally, with plasma functionalization CuO surface became highly hydrophilic and was attributed to the formation of polar surface groups. From XPS it was found that the polar nature of the CuO surface stem from the electrostatically bonded hydroxyl radicals. The enhance density of states at O2*p* region of the valence band indicating the probable formation of CuOOH at near surface region. This unique surface chemistry significantly reduces the onset potential for oxygen evolution reaction by 130 mV. Moreover, these plasma treated electrodes achieved 3 times the current density compared to standard annealed electrodes, 10 mA $cm^{-2}$ against 3 mA $cm^{-2}$ respectively at 1 V vs SCE in 0.1M KOH. It was demonstrated that the presence of oxygen in the plasma is necessary for the enhanced activities. The treated films also exhibited higher degree of dye adsorption and faster

degradation of Methylene Blue and Phenol under simulated solar light. This work presents potential opportunities to develop highly active catalysts for water splitting and organic pollutant degradation applications using atmospheric pressure functionalized thin films.

## 5. Acknowledgements

Satheesh Krishnamurthy acknowledges Recycling Lithium ion batteries for a sustainable technological and economic development (ReListed) DSTUKIERI-2018-19-008, Royal Society IES\R2\170272 and Royal Academy of Engineering and European commission Smart innovative system for recycling wastewater and creating closed loops in textile manufacturing industrial processes -958491 for the funding support. The authors acknowledge use of Zeiss Supra 55VP and JEOL 2100 supplied by the Electron Microscopy Suite, STEM, Open University

**References:**

[1] V.R. Stamenkovic, D. Strmcnik, P.P. Lopes, N.M. Markovic, Energy and fuels from electrochemical interfaces, Nat. Mater. 16 (2016) 57–69. https://doi.org/10.1038/nmat4738.

[2] Z.F. Huang, J. Song, Y. Du, S. Xi, S. Dou, J.M.V. Nsanzimana, C. Wang, Z.J. Xu, X. Wang, Chemical and structural origin of lattice oxygen oxidation in Co–Zn oxyhydroxide oxygen evolution electrocatalysts, Nat. Energy. 4 (2019) 329–338. https://doi.org/10.1038/s41560-019-0355-9.

[3] G. Li, S. Li, J. Ge, C. Liu, W. Xing, Discontinuously covered IrO2-RuO2@Ru electrocatalysts for the oxygen evolution reaction: How high activity and long-term durability can be simultaneously realized in the synergistic and hybrid nano-structure, J. Mater. Chem. A. 5 (2017) 17221–17229. https://doi.org/10.1039/c7ta05126c.

[4] T. Audichon, T.W. Napporn, C. Canaff, C. Morais, C. Comminges, K.B. Kokoh, IrO2 Coated on RuO2 as Efficient and Stable Electroactive Nanocatalysts for Electrochemical Water Splitting, J. Phys. Chem. C. 120 (2016) 2562–2573. https://doi.org/10.1021/acs.jpcc.5b11868.

[5] M.D. Kärkäs, B. Åkermark, Water oxidation using earth-abundant transition metal catalysts: Opportunities and challenges, Dalt. Trans. 45 (2016) 14421–14461. https://doi.org/10.1039/c6dt00809g.

[6] I. Roger, M.D. Symes, First row transition metal catalysts for solar-driven water

oxidation produced by electrodeposition, J. Mater. Chem. A. 4 (2016) 6724–6741. https://doi.org/10.1039/c5ta09423b.
[7] N.T. Suen, S.F. Hung, Q. Quan, N. Zhang, Y.J. Xu, H.M. Chen, Electrocatalysis for the oxygen evolution reaction: Recent development and future perspectives, Chem. Soc. Rev. 46 (2017) 337–365. https://doi.org/10.1039/c6cs00328a.
[8] M.B. Gawande, A. Goswami, F.-X.X. Felpin, T. Asefa, X. Huang, R. Silva, X. Zou, R. Zboril, R.S. Varma, Cu and Cu-Based Nanoparticles: Synthesis and Applications in Catalysis., Chem. Rev. 116 (2016) 3722–3811. https://doi.org/10.1021/acs.chemrev.5b00482.
[9] M.B. Gawande, A. Goswami, F.X. Felpin, T. Asefa, X. Huang, R. Silva, X. Zou, R. Zboril, R.S. Varma, Cu and Cu-Based Nanoparticles: Synthesis and Applications in Catalysis, Chem. Rev. 116 (2016) 3722–3811. https://doi.org/10.1021/acs.chemrev.5b00482.
[10] A. Roy, H.S. Jadhav, M. Cho, J.G. Seo, Electrochemical deposition of self-supported bifunctional copper oxide electrocatalyst for methanol oxidation and oxygen evolution reaction, J. Ind. Eng. Chem. 76 (2019) 515–523. https://doi.org/10.1016/j.jiec.2019.04.019.
[11] M.F. Al-Kuhaili, Characterization of copper oxide thin films deposited by the thermal evaporation of cuprous oxide (Cu2O), Vacuum. 82 (2008) 623–629. https://doi.org/10.1016/j.vacuum.2007.10.004.
[12] Y.F. Lim, C.S. Chua, C.J.J. Lee, D. Chi, Sol-gel deposited Cu2O and CuO thin films for photocatalytic water splitting, Phys. Chem. Chem. Phys. 16 (2014) 25928–25934. https://doi.org/10.1039/c4cp03241a.
[13] A.H. Jayatissa, K. Guo, A.C. Jayasuriya, Fabrication of cuprous and cupric oxide thin films by heat treatment, Appl. Surf. Sci. 255 (2009) 9474–9479. https://doi.org/10.1016/j.apsusc.2009.07.072.
[14] S. Masudy-Panah, R. Siavash Moakhar, C.S. Chua, H.R. Tan, T.I. Wong, D. Chi, G.K. Dalapati, Nanocrystal Engineering of Sputter-Grown CuO Photocathode for Visible-Light-Driven Electrochemical Water Splitting, ACS Appl. Mater. Interfaces. 8 (2016) 1206–1213. https://doi.org/10.1021/acsami.5b09613.
[15] X. Liu, S. Cui, Z. Sun, Y. Ren, X. Zhang, P. Du, Self-Supported Copper Oxide Electrocatalyst for Water Oxidation at Low Overpotential and Confirmation of Its Robustness by Cu K-Edge X-ray Absorption Spectroscopy, J. Phys. Chem. C. 120 (2016) 831–840. https://doi.org/10.1021/acs.jpcc.5b09818.
[16] S.M. Pawar, B.S. Pawar, B. Hou, J. Kim, A.T. Aqueel Ahmed, H.S. Chavan, Y. Jo, S. Cho, A.I. Inamdar, J.L. Gunjakar, H. Kim, S. Cha, H. Im, Self-assembled two-dimensional copper oxide nanosheet bundles as an efficient oxygen evolution reaction (OER) electrocatalyst for water splitting applications, J. Mater. Chem. A. 5 (2017) 12747–12751. https://doi.org/10.1039/c7ta02835k.
[17] S. Masudy-Panah, R. Siavash Moakhar, C.S. Chua, A. Kushwaha, T.I. Wong, G.K. Dalapati, Rapid thermal annealing assisted stability and efficiency enhancement in a sputter deposited CuO photocathode†, RSC Adv. 6 (2016) 29383–29390. https://doi.org/10.1039/c6ra03383k.
[18] H. Mistry, Y.W. Choi, A. Bagger, F. Scholten, C.S. Bonifacio, I. Sinev, N.J. Divins, I. Zegkinoglou, H.S. Jeon, K. Kisslinger, E.A. Stach, J.C. Yang, J. Rossmeisl, B. Roldan Cuenya, Enhanced Carbon Dioxide Electroreduction to Carbon Monoxide over Defect-Rich Plasma-Activated Silver Catalysts, Angew. Chemie - Int. Ed. 56 (2017) 11394–11398. https://doi.org/10.1002/anie.201704613.
[19] L. He, D. Zhou, Y. Lin, R. Ge, X. Hou, X. Sun, C. Zheng, Ultrarapid in Situ Synthesis of Cu2S Nanosheet Arrays on Copper Foam with Room-Temperature-Active Iodine

Plasma for Efficient and Cost-Effective Oxygen Evolution, ACS Catal. 8 (2018) 3859–3864. https://doi.org/10.1021/acscatal.8b00032.
[20] A. Altaweel, T. Gries, S. Migot, P. Boulet, A. Mézin, T. Belmonte, Localised growth of CuO nanowires by micro-afterglow oxidation at atmospheric pressure: Investigation of the role of stress, Surf. Coatings Technol. 305 (2016) 254–263. https://doi.org/10.1016/j.surfcoat.2016.08.001.
[21] H. Chen, Q. Zhao, L. Gao, J. Ran, Y. Hou, Water-Plasma Assisted Synthesis of Oxygen-Enriched Ni-Fe Layered Double Hydroxide Nanosheets for Efficient Oxygen Evolution Reaction, ACS Sustain. Chem. Eng. 7 (2019) 4247–4254. https://doi.org/10.1021/acssuschemeng.8b05953.
[22] L. Xu, Q. Jiang, Z. Xiao, X. Li, J. Huo, S. Wang, L. Dai, Plasma-Engraved Co3O4 Nanosheets with Oxygen Vacancies and High Surface Area for the Oxygen Evolution Reaction, Angew. Chemie - Int. Ed. 55 (2016) 5277–5281. https://doi.org/10.1002/anie.201600687.
[23] Y. Wang, C. Xie, Z. Zhang, D. Liu, R. Chen, S. Wang, In Situ Exfoliated, N-Doped, and Edge-Rich Ultrathin Layered Double Hydroxides Nanosheets for Oxygen Evolution Reaction, Adv. Funct. Mater. 28 (2018) 1703363. https://doi.org/10.1002/adfm.201703363.
[24] H. Mistry, A.S. Varela, C.S. Bonifacio, I. Zegkinoglou, I. Sinev, Y.W. Choi, K. Kisslinger, E.A. Stach, J.C. Yang, P. Strasser, B.R. Cuenya, Highly selective plasma-activated copper catalysts for carbon dioxide reduction to ethylene, Nat. Commun. 7 (2016) 1–9. https://doi.org/10.1038/ncomms12123.
[25] D. Gao, I. Zegkinoglou, N.J. Divins, F. Scholten, I. Sinev, P. Grosse, B. Roldan Cuenya, Plasma-Activated Copper Nanocube Catalysts for Efficient Carbon Dioxide Electroreduction to Hydrocarbons and Alcohols, ACS Nano. 11 (2017) 4825–4831. https://doi.org/10.1021/acsnano.7b01257.
[26] S. Dou, C.L. Dong, Z. Hu, Y.C. Huang, J.L. Chen, L. Tao, D. Yan, D. Chen, S. Shen, S. Chou, S. Wang, Atomic-Scale CoOx Species in Metal–Organic Frameworks for Oxygen Evolution Reaction, Adv. Funct. Mater. 27 (2017) 1702546. https://doi.org/10.1002/adfm.201702546.
[27] X. Lu, X. Yang, M. Tariq, F. Li, M. Steimecke, J. Li, A. Varga, M. Bron, B. Abel, Plasma-etched functionalized graphene as a metal-free electrode catalyst in solid acid fuel cells, J. Mater. Chem. A. 8 (2020) 2445–2452. https://doi.org/10.1039/c9ta10821a.
[28] A. Dey, A. Chroneos, N.S.J. Braithwaite, R.P. Gandhiraman, S. Krishnamurthy, Plasma engineering of graphene, Appl. Phys. Rev. 3 (2016) 021301. https://doi.org/10.1063/1.4947188.
[29] F. Yu, M. Liu, C. Ma, L. Di, B. Dai, L. Zhang, A review on the promising plasma-assisted preparation of electrocatalysts, Nanomaterials. 9 (2019). https://doi.org/10.3390/nano9101436.
[30] A. Dey, P. Ghosh, J. Bowen, N.S.J. Braithwaite, S. Krishnamurthy, Engineering work function of graphene oxide from p to n type using a low power atmospheric pressure plasma jet, Phys. Chem. Chem. Phys. 22 (2020) 7685–7698. https://doi.org/10.1039/c9cp06174f.
[31] A. Dey, A. Lopez, G. Filipič, A. Jayan, D. Nordlund, J. Koehne, S. Krishnamurthy, R.P. Gandhiraman, M. Meyyappan, Plasma jet based in situ reduction of copper oxide in direct write printing, J. Vac. Sci. Technol. B. 37 (2019) 031203. https://doi.org/10.1116/1.5087255.
[32] A. Xu, C. Dong, A. Wu, R. Li, L. Wang, D.D. MacDonald, X. Li, Plasma-modified C-doped Co 3 O 4 nanosheets for the oxygen evolution reaction designed by Butler-

Volmer and first-principle calculations, J. Mater. Chem. A. 7 (2019) 4581–4595. https://doi.org/10.1039/c8ta11424b.
[33] A. Dey, G. Chandrabose, L.A.O. Damptey, E.S. Erakulan, R. Thapa, S. Zhuk, G.K. Dalapati, S. Ramakrishna, N.S.J. Braithwaite, A. Shirzadi, S. Krishnamurthy, Cu2O/CuO heterojunction catalysts through atmospheric pressure plasma induced defect passivation, Appl. Surf. Sci. 541 (2021) 148571. https://doi.org/10.1016/j.apsusc.2020.148571.
[34] X. An, C. Yang, Z. Wu, L. Liu, S. Li, L. Zhou, W. Tang, Z. Ma, Z. Wu, R.K.Y. Fu, X. Tian, H. Lin, F. Pan, P.K. Chu, Self-Regulated Super-Hydrophobic Cu/CuO Electrode Film Deposited by One-Step High-Power Sputtering, Adv. Electron. Mater. 6 (2020) 1900891. https://doi.org/10.1002/aelm.201900891.
[35] J. Wu, K. Yin, M. Li, Z. Wu, S. Xiao, H. Wang, J.A. Duan, J. He, Under-oil self-driven and directional transport of water on a femtosecond laser-processed superhydrophilic geometry-gradient structure, Nanoscale. 12 (2020) 4077–4084. https://doi.org/10.1039/c9nr09902f.
[36] F.Z. Zhang, R.A. Winholtz, W.J. Black, M.R. Wilson, H. Taub, H.B. Ma, Effect of Hydrophilic Nanostructured Cupric Oxide Surfaces on the Heat Transport Capability of a Flat-Plate Oscillating Heat Pipe, J. Heat Transfer. 138 (2016). https://doi.org/10.1115/1.4032608.
[37] H. Zhang, L. Li, B. Jiang, Q. Zhang, J. Ma, D. Tang, Y. Song, Highly Thermally Insulated and Superhydrophilic Corn Straw for Efficient Solar Vapor Generation, ACS Appl. Mater. Interfaces. 12 (2020) 16503–16511. https://doi.org/10.1021/acsami.0c01585.
[38] S. Olveira, A. Stojanovic, S. Seeger, Superhydrophilic and Superamphiphilic Coatings, in: Funct. Polym. Coatings, John Wiley & Sons, Inc, Hoboken, NJ, 2015: pp. 96–132. https://doi.org/10.1002/9781118883051.ch3.
[39] D. Chen, Z. Kang, W. Li, One-step electrodeposition to fabricate superhydrophobic coating and its reversible wettability transformation, Mater. Res. Express. 7 (2019). https://doi.org/10.1088/2053-1591/ab5bf3.
[40] A. Chaudhary, H.C. Barshilia, Nanometric multiscale rough CuO/Cu(OH)2 superhydrophobic surfaces prepared by a facile one-step solution-immersion process: Transition to superhydrophilicity with oxygen plasma treatment, J. Phys. Chem. C. 115 (2011) 18213–18220. https://doi.org/10.1021/jp204439c.
[41] S. Zhuk, T.K.S. Wong, M. Petrović, E. Kymakis, S.S. Hadke, S. Lie, L.H. Wong, P. Sonar, A. Dey, S. Krishnamurthy, G.K. Dalapati, Solution Processed Pure Sulfide CZCTS Solar Cells with Efficiency 10.8% using Ultra-Thin CuO Intermediate Layer, Sol. RRL. (2020). https://doi.org/10.1002/solr.202000293.
[42] J. Golda, J. Held, B. Redeker, M. Konkowski, P. Beijer, A. Sobota, G. Kroesen, N.S.J. Braithwaite, S. Reuter, M.M. Turner, T. Gans, D. O'Connell, V. Schulz-Von Der Gathen, Concepts and characteristics of the "COST Reference Microplasma Jet," J. Phys. D. Appl. Phys. 49 (2016) 084003. https://doi.org/10.1088/0022-3727/49/8/084003.
[43] O. Müller, M. Nachtegaal, J. Just, D. Lützenkirchen-Hecht, R. Frahm, Quick-EXAFS setup at the SuperXAS beamline for in situ X-ray absorption spectroscopy with 10ms time resolution, in: J. Synchrotron Radiat., International Union of Crystallography, 2016: pp. 260–266. https://doi.org/10.1107/S1600577515018007.
[44] A.H. Clark, P. Steiger, B. Bornmann, S. Hitz, R. Frahm, D. Ferri, M. Nachtegaal, Fluorescence-detected quick-scanning X-ray absorption spectroscopy, J. Synchrotron Radiat. 27 (2020) 681–688. https://doi.org/10.1107/S1600577520002350.
[45] A.H. Clark, J. Imbao, R. Frahm, M. Nachtegaal, ProQEXAFS: A highly optimized

parallelized rapid processing software for QEXAFS data, J. Synchrotron Radiat. 27 (2020) 551–557. https://doi.org/10.1107/S1600577519017053.
[46] B. Ravel, M. Newville, ATHENA, ARTEMIS, HEPHAESTUS: Data analysis for X-ray absorption spectroscopy using IFEFFIT, in: J. Synchrotron Radiat., International Union of Crystallography, 2005: pp. 537–541. https://doi.org/10.1107/S0909049505012719.
[47] G. Sakuma, Y. Fukunaka, H. Matsushima, Nucleation and growth of electrolytic gas bubbles under microgravity, Int. J. Hydrogen Energy. 39 (2014) 7638–7645. https://doi.org/10.1016/j.ijhydene.2014.03.059.
[48] C. Meng, B. Wang, Z. Gao, Z. Liu, Q. Zhang, J. Zhai, Insight into the Role of Surface Wettability in Electrocatalytic Hydrogen Evolution Reactions Using Light-Sensitive Nanotubular TiO 2 Supported Pt Electrodes, Sci. Rep. 7 (2017) 1–8. https://doi.org/10.1038/srep41825.
[49] K.A. Stoerzinger, W.T. Hong, G. Azimi, L. Giordano, Y.L. Lee, E.J. Crumlin, M.D. Biegalski, H. Bluhm, K.K. Varanasi, Y. Shao-Horn, Reactivity of Perovskites with Water: Role of Hydroxylation in Wetting and Implications for Oxygen Electrocatalysis, J. Phys. Chem. C. 119 (2015) 18504–18512. https://doi.org/10.1021/acs.jpcc.5b06621.
[50] C.M. Ding, M.L. Lv, Y. Zhu, L. Jiang, H. Liu, Wettability-regulated extracellular electron transfer from the living organism of shewanella loihica PV-4, Angew. Chemie - Int. Ed. 54 (2015) 1446–1451. https://doi.org/10.1002/anie.201409163.
[51] X. Shan, J. Liu, H. Mu, Y. Xiao, B. Mei, W. Liu, G. Lin, Z. Jiang, L. Wen, L. Jiang, An Engineered Superhydrophilic/Superaerophobic Electrocatalyst Composed of the Supported CoMoSx Chalcogel for Overall Water Splitting, Angew. Chemie - Int. Ed. 59 (2020) 1659–1665. https://doi.org/10.1002/anie.201911617.
[52] J. Li, X. Gao, Z. Li, J. Wang, L. Zhu, C. Yin, Y. Wang, X. Li, Z. Liu, J. Zhang, C. Tung, L. Wu, Superhydrophilic Graphdiyne Accelerates Interfacial Mass/Electron Transportation to Boost Electrocatalytic and Photoelectrocatalytic Water Oxidation Activity, Adv. Funct. Mater. 29 (2019) 1808079. https://doi.org/10.1002/adfm.201808079.
[53] J. Li, X. Jin, R. Li, Y. Zhao, X. Wang, X. Liu, H. Jiao, Copper oxide nanowires for efficient photoelectrochemical water splitting, Appl. Catal. B Environ. 240 (2019) 1–8. https://doi.org/10.1016/j.apcatb.2018.08.070.
[54] C.R. Crick, I.P. Parkin, A single step route to superhydrophobic surfaces through aerosol assisted deposition of rough polymer surfaces: Duplicating the lotus effect, J. Mater. Chem. 19 (2009) 1074–1076. https://doi.org/10.1039/b820102c.
[55] C.R. Crick, I.P. Parkin, Preparation and Characterisation of Super-Hydrophobic Surfaces, Chem. - A Eur. J. 16 (2010) 3568–3588. https://doi.org/10.1002/chem.200903335.
[56] S. Li, K. Page, S. Sathasivam, F. Heale, G. He, Y. Lu, Y. Lai, G. Chen, C.J. Carmalt, I.P. Parkin, Efficiently texturing hierarchical superhydrophobic fluoride-free translucent films by AACVD with excellent durability and self-cleaning ability, J. Mater. Chem. A. 6 (2018) 17633–17641. https://doi.org/10.1039/c8ta05402a.
[57] G. Filipič, U. Cvelbar, Copper oxide nanowires: a review of growth, Nanotechnology. 23 (2012) 194001. https://doi.org/10.1088/0957-4484/23/19/194001.
[58] A.A. Dubale, W.N. Su, A.G. Tamirat, C.J. Pan, B.A. Aragaw, H.M. Chen, C.H. Chen, B.J. Hwang, The synergetic effect of graphene on Cu2O nanowire arrays as a highly efficient hydrogen evolution photocathode in water splitting, J. Mater. Chem. A. 2 (2014) 18383–18397. https://doi.org/10.1039/c4ta03464c.
[59] X. Zou, H. Fan, Y. Tian, M. Zhang, X. Yan, Chemical bath deposition of Cu2O

quantum dots onto ZnO nanorod arrays for application in photovoltaic devices, RSC Adv. 5 (2015) 23401–23409. https://doi.org/10.1039/c4ra13776k.
[60] K.P. Sapkota, I. Lee, M.A. Hanif, M.A. Islam, J. Akter, J.R. Hahn, Enhanced Visible-Light Photocatalysis of Nanocomposites of Copper Oxide and Single-Walled Carbon Nanotubes for the Degradation of Methylene Blue, Catalysts. 10 (2020) 297.
[61] S. Velu, K. Suzuki, M. Vijayaraj, S. Barman, C.S. Gopinath, In situ XPS investigations of Cu1-xNixZnAl-mixed metal oxide catalysts used in the oxidative steam reforming of bio-ethanol, Appl. Catal. B Environ. 55 (2005) 287–299. https://doi.org/10.1016/j.apcatb.2004.09.007.
[62] J. Park, K. Lim, R.D. Ramsier, Y.C. Kang, Spectroscopic and morphological investigation of copper oxide thin films prepared by magnetron sputtering at various oxygen ratios, Bull. Korean Chem. Soc. 32 (2011) 3395–3399. https://doi.org/10.5012/bkcs.2011.32.9.3395.
[63] M.C. Biesinger, Advanced analysis of copper X-ray photoelectron spectra, Surf. Interface Anal. 49 (2017) 1325–1334. https://doi.org/10.1002/sia.6239.
[64] A. Gaur, D. Shrivastava, K. Joshi, Copper K-edge XANES of Cu(I) and Cu(II) oxide mixtures, J. Phys. Conf. Ser. 190 (2009). https://doi.org/10.1088/1742-6596/190/1/012084.
[65] A. Sharma, M. Varshney, J. Park, T.K. Ha, K.H. Chae, H.J. Shin, XANES, EXAFS and photocatalytic investigations on copper oxide nanoparticles and nanocomposites, RSC Adv. 5 (2015) 21762–21771. https://doi.org/10.1039/c4ra16217j.
[66] R.P. Wijesundera, M. Hidaka, K. Koga, M. Sakai, W. Siripala, J.Y. Choi, N.E. Sung, Effects of annealing on the properties and structure of electrodeposited semiconducting Cu-O thin films, Phys. Status Solidi Basic Res. 244 (2007) 4629–4642. https://doi.org/10.1002/pssb.200743275.
[67] A. Ahmed, P. Elvati, A. Violi, Size-and phase-dependent structure of copper( ii ) oxide nanoparticles, RSC Adv. 5 (2015) 35033–35041. https://doi.org/10.1039/C5RA04276C.
[68] M. Abdel Rafea, N. Roushdy, Determination of the optical band gap for amorphous and nanocrystalline copper oxide thin films prepared by SILAR technique, J. Phys. D. Appl. Phys. 42 (2009). https://doi.org/10.1088/0022-3727/42/1/015413.
[69] S. Masudy-Panah, R. Siavash Moakhar, C.S. Chua, A. Kushwaha, G.K. Dalapati, Stable and Efficient CuO Based Photocathode through Oxygen-Rich Composition and Au-Pd Nanostructure Incorporation for Solar-Hydrogen Production, ACS Appl. Mater. Interfaces. 9 (2017) 27596–27606. https://doi.org/10.1021/acsami.7b02685.
[70] J. Feng, J. Zhu, W. Lv, J. Li, W. Yan, Effect of hydroxyl group of carboxylic acids on the adsorption of Acid Red G and Methylene Blue on TiO2, Chem. Eng. J. 269 (2015) 316–322. https://doi.org/10.1016/j.cej.2015.01.109.
[71] C. Feng, Z. Chen, J. Jing, J. Hou, The photocatalytic phenol degradation mechanism of Ag-modified ZnO nanorods, J. Mater. Chem. C. 8 (2020) 3000–3009. https://doi.org/10.1039/c9tc05010h.
[72] C.G. Vayenas, S. Bebelis, S. Ladas, Dependence of catalytic rates on catalyst work function, Nature. 343 (1990) 625–627. https://doi.org/10.1038/343625a0.
[73] Y. Yang, D. Xu, Q. Wu, P. Diao, Cu2O/CuO bilayered composite as a high-efficiency photocathode for photoelectrochemical hydrogen evolution reaction, Sci. Rep. 6 (2016) 35158. https://doi.org/10.1038/srep35158.
[74] R. Katal, S. Masudy-panah, E.Y.J. Kong, N. Dasineh Khiavi, M.H.D. Abadi Farahani, X. Gong, Nanocrystal-engineered thin CuO film photocatalyst for visible-light-driven photocatalytic degradation of organic pollutant in aqueous solution, Catal. Today. 340 (2020) 236–244. https://doi.org/10.1016/j.cattod.2018.12.019.

[75] S. Sai Guru Srinivasan, B. Govardhanan, P. Aabel, M. Ashok, M.C. Santhosh Kumar, Effect of oxygen partial pressure on the tuning of copper oxide thin films by reactive sputtering for solar light driven photocatalysis, Sol. Energy. 187 (2019) 368–378. https://doi.org/10.1016/j.solener.2019.05.057.
[76] A.A. Al-Ghamdi, M.H. Khedr, M. Shahnawaze Ansari, P.M.Z. Hasan, M.S. Abdel-Wahab, A.A. Farghali, RF sputtered CuO thin films: Structural, optical and photo-catalytic behavior, Phys. E Low-Dimensional Syst. Nanostructures. 81 (2016) 83–90. https://doi.org/10.1016/j.physe.2016.03.004.
[77] N.D. Khiavi, R. Katal, S.K. Eshkalak, S. Masudy-Panah, S. Ramakrishna, H. Jiangyong, Visible light driven heterojunction photocatalyst of cuo-cu2o thin films for photocatalytic degradation of organic pollutants, Nanomaterials. 9 (2019). https://doi.org/10.3390/nano9071011.
[78] K. Sahu, S. Choudhary, S.A. Khan, A. Pandey, S. Mohapatra, Thermal evolution of morphological, structural, optical and photocatalytic properties of CuO thin films, Nano-Structures and Nano-Objects. 17 (2019) 92–102. https://doi.org/10.1016/j.nanoso.2018.12.005.
[79] K. Sahu, S. Choudhary, S. Mohapatra, Fabrication of Au-CuO hybrid plasmonic nanostructured thin films with enhanced photocatalytic activity, Mater. Res. Bull. 123 (2020) 110707. https://doi.org/10.1016/j.materresbull.2019.110707.
[80] W.M.A. El Rouby, A.A. Al-Ghamdi, M.S. Abdel-Wahab, A. Jilani, Sunlight-enhanced catalytic degradation over Ag-CuO nanoparticles thin films prepared by DC/RF sputtering technique, Bull. Mater. Sci. 41 (2018) 58. https://doi.org/10.1007/s12034-018-1548-8.
[81] J. Singh, A.K. Manna, R.K. Soni, Sunlight driven photocatalysis and non-enzymatic glucose sensing performance of cubic structured CuO thin films, Appl. Surf. Sci. 530 (2020) 147258. https://doi.org/10.1016/j.apsusc.2020.147258.